

# Ambient Noise Tomography for Sub-Regional Mineral Exploration Using Nodal MEMS Accelerometers: A Case Study from the Kansanshi Cu-Au Mine, Zambia.

T. Mackay-Champion<sup>1</sup>, N. Harmon<sup>2</sup>, S. Mutelekesha<sup>3</sup>, M. Chanda<sup>4</sup>, T. Hudson<sup>5</sup>, J.-M. Kendall<sup>1</sup>, M.C. Daly<sup>1</sup>.

1. Department of Earth Sciences, University of Oxford, South Parks Road, Oxford, UK.

2. Geology and Geophysics, Woods Hole Oceanographic Institution, Woods Hole, Massachusetts 02543, USA, Woods Hole Oceanographic Institute, USA.

3. First Quantum Minerals Ltd.

4. Geological Survey Department, Ministry of Mines, Zambia.

5. Institute of Geophysics, ETH Zürich, Switzerland.

## Abstract

Metals are essential to the success of the energy transition, but the discovery rate of deposits has been in decline. Innovative new methods of exploration are required. In recent years, Ambient Noise Tomography (ANT) using passive seismic wavefields recovered from the background noise recorded by seismometers has gained increasing popularity as a tool in mineral exploration, with many studies demonstrating its efficacy in mapping the local geological structure of mineral deposits. However, these studies have been limited to depths of a few hundred meters to a few kilometers and have focused on small lateral scales. As such, the application of ANT for regional to sub-regional (tens of kilometers) exploration has remained untested. In this study, a network of 30 Sercel WiNG MEMS accelerometers was deployed along a c. 50 km NE-SW line through the Kansanshi copper (Cu) – gold (Au) mine. The Kansanshi mine, owned by First Quantum Minerals (Ltd.), is the third largest copper mine in Africa, with a resource of 982.3 Mt of Cu (using a cut-off grade of TCu 0.2 %) and 0.11g/tonne of Au as of December 2023. Here we show that ANT performed with cost-effective MEMS accelerometers can identify a significant body of metal source sediments beneath Kansanshi, with a thickness of multiple kilometres, as well as structures consistent with the expulsion of mineralizing fluid through focused zones. These results demonstrate that ANT performed with MEMS accelerometers would be a valuable tool for sub-regional mineral exploration of greenfield sites.

## 1. Introduction

The fundamental importance of metals such as copper (Cu), nickel, lithium, and cobalt to electricity transmission and battery technology has seen them become critical components of the energy transition to a Net Zero future. However, S&P Global Market Intelligence have estimated a 20 million tonne deficit in Cu by 2035 as global electrification increases demand. This problem is exacerbated by the declining effectiveness of mineral exploration programs. The discovery rate of deposits has been in decline over the past thirty years (Okada, 2021), and the recent growth of exploration budgets has not led to a meaningful increase in the number of major discoveries (White & Hook, 2023; McKeith et al., 2010).

Given these circumstances, developing innovative methods for metal exploration and advancing tools and techniques for discovering and defining subsurface deposits is essential

(Wood & Hedenquist, 2019; Watzel, 2023). In recent years, ambient noise tomography has been increasing in popularity as a tool in mineral exploration. A number of studies have proved its efficacy for understanding the local geological structure of mineral deposits (e.g., Colombero et al., 2022) and the significant role this technique will play in mineral exploration was recently documented by Reid et al. (2025). However, up until now these studies have focused on the upper 100s metres to the top couple of km and on a limited lateral scale. While this provides valuable insights into the formation mechanisms of a deposit on a local scale, it is of limited use when exploring for new deposits or attempting to understand the geological systems controlling the location of deposits at a regional to sub-regional (10s kilometres) scale. In this study, we show that ambient noise tomography using nodal Micro-ElectroMechanical System (MEMS) accelerometers can be used to understand the crustal structure of a sub-regional area and thus to vector towards areas which show promise for mineral exploration.

To test this hypothesis, a network of 30 Sercel WiNG MEMS accelerometers was deployed along a c. 50 km NE-SW line through the Kansanshi copper (Cu) – gold (Au) mine. The Kansanshi mine, owned by First Quantum Minerals (Ltd.), is the third largest copper mine in Africa, with a resource of 982.3 Mt of Cu (using a cut-off grade of TCu 0.2 %) and 0.11g/tonne of Au as of December 2023. It is therefore classified as a supergiant deposit (i.e., > 24 Mt contained Cu). The mine is located approximately 10 km north of Solwezi, Zambia, and is hosted within the Central African Copperbelt (CACB). The CACB comprises the Neoproterozoic Katangan Basin, which is one of three basins worldwide to host supergiant Cu deposits, the two others being the Permian Zechstein basin of Europe (Vaughan et al., 1989), and the Paleoproterozoic Kodaro-Udokan basin of Siberia (Bakun et al., 1966). The CACB contributes about 14% and 60% of the world's supply of copper and cobalt (Selley et al., 2005)

Kansanshi is a sediment-hosted Cu deposit. Sediment-hosted Cu deposits currently account for ~ 23 % of the world's Cu production (Hitzman et al., 2005) and largely comprise relatively thin (< 30 m) zones of disseminated and veinlet Cu-sulphides that occur concordant with lithological layering within sedimentary basins (Hitzman et al., 2010). The deposits occur within a variety of sedimentary rock types but are generally found at or near the contact between red-bed sequences and overlying shales, siltstones or carbonates (Hitzman et al. 2010). Hitzman et al. (2010) described four important controls on the formation of significant sediment-hosted metal deposits: 1) the presence of metal source sediments, 2) the presence of reduced sediments to serve as chemical traps, 3) saline brines for leaching and transporting metals, and 4) the expulsion of mineralizing fluids through focused zones. However, it is unclear how important these four controls were for the formation of Kansanshi, as the deposit is atypical of deposits in the CACB for two reasons. Firstly, the deposit is hosted within relatively high-grade, garnet- and kyanite-bearing metasediments as opposed to undeformed sediments (Barron, 2003). Secondly, the deposit contains metre-wide, cross-cutting, high-grade veins which contain approximately 30% of the resource.

Consequently, this study seeks to answer two key questions: (1) To what extent does the Kansanshi deposit align with the conditions outlined in the Hitzman et al. model? (2) Could Ambient Noise Tomography (ANT) have identified the Kansanshi deposit without prior constraints?

## 1.1. Instrumentation

Ambient noise tomography was first used a couple of decades ago to understand the crustal structure of the western United States of America (Shapiro et al., 2005). Since then, it has been used at a variety of scales from continental down to experiments on the 100s metres scale (e.g., Stork et al., 2018). Broadly, the larger-scale ANT studies have relied upon conventional broadband seismometers such as Guralp ESPCDs which are expensive (> £10,000 per unit), highly technical and only ever deployed in relatively low numbers (typically  $n < 30$ ). These large-scale studies use low frequency seismic waves (< 0.1 Hz) to which these conventional instruments are particularly sensitive. Smaller scale studies have predominantly relied upon simple induction geophones and used relatively high frequencies (> 1 Hz). The corner frequencies of these geophones are often approximately 4 Hz and as such, are typically not deployed to examine frequencies below 1 Hz.

MEMS accelerometers operate using electronic force-balance systems, which function by measuring the voltage required to maintain a positive electrode in a fixed position between two negative electrodes (Herrmann et al., 2021; Liu et al., 2022). These sensors measure acceleration and offer several advantages over conventional instruments. Their lightweight and compact design facilitates the deployment of large networks or arrays, while their sensitivity to external factors like temperature is an order of magnitude lower than that of standard geophones (Laine & Mougenot, 2014). Additionally, MEMS accelerometers do not exhibit the data jitter commonly observed in geophones (Herrmann et al., 2021), and the instrument response remains constant across the frequency spectrum (Tellier et al., 2020). They are cost-effective and can be relied upon to record signals < 1 Hz (Fougerat et al., 2018). For this reason, the advent of MEMS accelerometers with low noise floors provides the opportunity for low frequency, large-scale studies with larger numbers of stations and logically easy deployments. These characteristics make MEMS accelerometers ideal for the exploration industry and is why these instruments were used in this study.

## 1.2. Geological setting of the Kansanshi deposit

The Kansanshi deposit is a sediment-hosted Cu deposit. Sediment-hosted Cu deposits account for c. 23 % of the world's Cu production (Hitzman et al., 2005). The deposit is hosted within the Domes Region of the Neoproterozoic Katangan Basin which crops out in Zambia and southern Democratic Republic of the Congo. The basin is bordered to the north by the Archaean Congo Craton, to the east by the Paleoproterozoic Banguweulu Block and the Mesoproterozoic Irumide Belt, and to the south by the Archaean Kalahari Craton (Figure 1). The Domes Region of the basin is characterised by amphibolite-facies metamorphism and recumbent folding (Cosi et al., 1992). The metasedimentary rocks at Kansanshi can be divided into two key domains, following Daly & Tosca (2020): (1) an autochthonous package of gneissic and schistose basement overlain by 1-2 km of Lower Roan quartzites, metaconglomerates and Upper Roan metacarbonates, (2) an overlying allochthonous metamorphic sheet containing biotite- and garnet-grade schists. The base of this allochthonous sheet is the Kansanshi Thrust, which runs along the contact of Mwashia Group sediments and underlying Upper Roan metacarbonates. The Kansanshi deposit is found within the allochthonous metamorphic sheet and comprises two main types of mineralization: stratabound and vein. The stratabound mineralization hosts the majority of Kansanshi's copper metal and is predominantly found as bedding-parallel disseminated chalcopyrite within phyllites, accompanied by lesser amounts of bornite and molybdenite. Vein mineralization hosts more than 30 % of the Cu metal and are typically composed of

quartz or carbonate with accessory chalcopyrite, malachite, and chalcocite. The veins can be up to several metres wide and typically exhibit sub-vertical, cross-cutting orientations (Kansanshi Operations, NI 43-101 Technical Report, July 2024). The metamorphic character of the rocks in Kansanshi is at odds with traditional sediment-hosted deposits, which typically occur at the contact between unmetamorphosed red-bed sequences and overlying shales, siltstones or carbonates (Hitzman et al. 2010).

## 2. Ambient Noise Tomography Method

Ambient Noise Tomography (ANT) uses the difference in phase between ambient surface waves travelling through an array to examine the 3-D seismic velocity structure within the array. These surface waves can be generated by distant earthquakes, by the oceans, or by more local sources such as mine-blasts. The phase difference of these surface waves between different pairs of stations is calculated using cross-correlations of the ambient recordings of each station within the array. The range of surface-wave frequencies recorded by the array is important. The depth of highest resolution for a given surface wave is proportional to its frequency - a lower frequency wave will have sensitivity to greater depths. This study follows the ANT method outlined in Harmon & Rychert (2016). Here we use Rayleigh Waves revealed by ambient noise cross-correlations to create a 44 km long, 2-dimensional (2-D) shear-wave velocity cross-section through the Kansanshi Mine and the surrounding terrane. Towards these ends, we perform a two-step inversion: the initial inversion generates phase velocity maps for surface waves at specific periods within the study area using the cross-correlations. The second inversion generates 1-dimensional (1-D) shear-wave (S-wave) velocity models from the 1-D phase velocity dispersion curves created using the phase velocity maps. These 1-D S-wave models are stitched together to create a final 2-D cross-section. The workflow is outlined below.

### 2.1. *Deployment, cross-correlations and phase velocity measurements*

A network of 30 Sercel WiNG nodal MEMS accelerometers was deployed along a c. 50 km long, linear transect through the Kansanshi Cu-mine and Solwezi, Zambia between October 2021 and May 2022, for a total of 188 days (Figure 2). Each station was approximately 1.5-2 km from its nearest neighbour. The WiNG instrument contains a vertical-component Micro ElectroMechanical Systems (MEMS) accelerometer and an internal GPS and battery system. Each instrument weighs approximately 780 g, has a battery life of 40-50 days, and is well suited to recording seismic data below 1 Hz (Fougerat et al., 2018).

The ambient recordings of each accelerometer were down sampled from the original sample rate of 500 Hz to 4 Hz. One-bit amplitude normalization and spectral whitening were then performed on the down sampled data, following Bensen et al. (2007). Finally, the processed data were binned into 4-hour time windows. The cross-correlation of the seismograms for every possible pair of stations in the network was then calculated for each time window, followed by a linear stack across all of the time windows. For a network of 30 stations, this resulted in 420 final cross-correlation pairs. The cross-correlations provide an estimate of the empirical Green's function and therefore provide information on the velocity structure between each pair of stations.

For each frequency of interest, the average surface-wave phase velocity within the array,  $\bar{c}$ , was calculated by finding the phase velocity with the lowest data residual between the phase calculated for a zero-order Bessel Function of the first kind and the observed phase of the real (symmetric) component of all the cross-correlations. The Bessel function is a component of the empirical Green's Function for a surface wave (Sanchez-Sesma & Campillo, 1991); Harmon et al., 2008). This was performed for periods of 2.5s, 3.5s, 4.5s, 5.5s, 6.5, and 7.0s (Figure 4).

The total phase,  $\phi_T$ , for each pair of stations was then estimated by unwrapping the phase of the Fourier transformed cross-correlations, using the average phase velocity calculated above to provide an initial estimate of the total number of wavelengths between the pair of stations (Equation 1). It is assumed that the “true” total phase lies within a single wavelength of the total phase calculated with the average phase velocity.

$$\phi_T = \phi_{CC} + 2\pi N + \frac{\pi}{4} \quad (1)$$

$$\left| \phi_T - \frac{2\pi s}{\bar{c}p} \right| < 2\pi \quad (2)$$

Where  $N$  is the integer number of wavelengths between the pair of stations,  $\phi_{CC}$  is the phase of the cross-correlation,  $\frac{\pi}{4}$  is the phase correction required for the great circle path (Harmon et al., 2008),  $s$  is the interstation distance and  $p$  is the period of interest.

## 2.2. Phase velocity inversion

The total phase from all useable station pairs is inverted for network-wide 2-D phase velocity maps using an iterative damped, weighted least-squares inversion, following Forsyth & Li, 2005, and further studies such as Harmon & Rychert (2016) and Schlaphorst et al. (2021).

The total phase is converted into an observed phase residual relative to the calculated phase assuming the average phase velocity,  $\bar{c}$ . This observed residual,  $\delta\phi$ , is the data used within the tomography (Equation 3).

$$\delta\phi = \phi_T - \frac{2\pi s}{\bar{c}p} \quad (3)$$

Where  $p$  is the period of interest and  $s$  is the inter-station distance. We treat the data as a normally distributed random variable with uncorrelated uncertainty. As such, the *a priori* data covariance matrix,  $C_d$ , is a diagonal matrix with a constant value of 0.2, following Forsyth & Lin (2005) and Harmon & Rychert (2016).

A gridded nodal parameterisation was used for the model,  $m$ . The resulting phase velocity map is a weighted average of the phase velocities at each model node. The initial model,  $m_0$ , is uniformly set to the average phase velocity,  $\bar{c}$ . Damping of the inversion is achieved using the *a priori* model covariance matrix,  $C_m$ , which uses a minimum length criterion and thus contains only diagonal terms (Marquardt, 1970).

$$C_m = \epsilon^2 W_m \quad (4)$$

Where  $W_m$  is a diagonal weighting matrix quantifying the relative importance of the solution length for each point in the velocity model and  $\epsilon$  is a damping parameter controlling the balance between prediction error and the solution length. We employ a uniform variance for all points in the interior of the grid. An outer boundary layer of nodes is also included with a ten-fold higher variance, such that these essentially undamped outer nodes can "absorb" variations that represent additional deviations from the idealized modeling assumptions (Forsyth & Li, 2005). The damping parameter  $\epsilon$  was assigned a value of 0.2 using an L-curve analysis (Figure Supp1). The observations (observed residual phase) are related to the model (phase velocity) assuming the following model:

$$d = \delta\phi = \iint K \frac{\delta c}{c} dx dy \quad (5)$$

$$G = \iint K dx dy \quad (6)$$

Where  $K$  is the 2-D finite frequency phase sensitivity kernels of Zhou et al. (2004) and  $\delta c = c - \bar{c}$  (i.e., the change in phase velocity relative to the starting model at a particular point in  $x$  and  $y$ ). In essence, the inversion determines the change in phase velocity,  $\delta c$ , needed from the initial model to account for the observed phase residual,  $\delta\phi$ . This is achieved by iterating (*i*) over Equations 7 –98.

$$\Delta d = d - G(m(i) - m_0) \quad (7)$$

$$\Delta m = \left( G^T C_d^{-1} G + C_m^{-1} \right)^{-1} \left( G^T C_d^{-1} \Delta d \right) \quad (8)$$

$$m(i + 1) = m(i) + \Delta m \quad (9)$$

We find that the best-fit model is typically found after 11 iterations, as defined by a plateauing in the variance of the residuals ( $\epsilon = d - G\Delta m$ ). Following the inversion, a smoothing is performed using a 2-D Gaussian weighting function, in which the phase velocity values within a high-resolution grid are defined as the weighted average of the phase velocities at each point in the model grid ( $m_k$ ). This follows the method of Forsyth & Lin (2005). The Gaussian functions are scaled with distance, such that proximal model nodes exert more weight on the value than distal model node. This smoothing allows the velocity to be continuously described everywhere in the area of interest, rather than solely at discrete model nodes. The length-scale of the smoothing is controlled by the "characteristic length",  $L_w$ , which controls the width of the Gaussian function. There is no absolute criterion for selecting the characteristic length, which causes a trade-off between data misfit and model length. Instead, a conventional trade-off curve analysis was performed, and a value of 5.5 km was assigned for  $L_w$ . The error, amplitude resolution, spatial resolution, and phase velocity residuals for each inversion were calculated using the methods outlined in the Supplementary Information.

### 2.3. S-wave velocity inversion

Shear wave (S-wave) velocity models were created by first generating 1-D dispersion curves at all points of interest. The dispersion curves were created using the 2-D phase velocity tomography maps. These curves were then inverted for 1-D S-wave velocity with depth using an iterative non-linear least-squares approach. We use Computer Programs in Seismology to forward calculate ( $F(m)$ ) the dispersion and sensitivity kernels for each method (Herrmann, 2013). The density and  $V_p/V_s$  of the inversion are fixed at 2.7 kg/m<sup>3</sup> and 1.7 respectively.

The iterative non-linear least-squares approach iteratively updates the S-wave model,  $m$ , through Equations 10 – 13, to minimize the misfit between the observed phase velocities are those predicted for the model ( $\Delta d$ ). We perform 100 iterations for each model.

$$\Delta d = d^{obs} - d^{pred} \quad (10)$$

$$\Delta m = \left( G^T C_d^{-1} G + C_m \right)^{-1} \left( G^T C_d^{-1} \Delta d \right) \quad (11)$$

$$m(i+1) = m(i) + \Delta m \quad (12)$$

$$[d^{pred}(i+1), G(i+1)] = F(m(i+1)) \quad (13)$$

At the end of each loop, the forward model dispersion curves and sensitivity kernels are re-calculated because the sensitivity kernels are a function of the model (hence the inversion is non-linear). This follows the method of Tarantola & Valette (1982) as employed in Harmon & Rychert (2016). The problem is damped using diagonal terms in the model covariance matrix ( $C_m$ ) equal to 0.1, following a trial-and-error assessing the fit of the model to the data and the smoothness of the model. The quality of the model is quantified using a chi-squared objective function (Equation 14).

$$\chi = \frac{1}{N} \sum_{i=1}^N \left( \frac{d_i^{obs} - d_i^{pred}}{2\sigma_i} \right)^2 \quad (14)$$

Where  $N$  is the number of periods included in the inversion. A value above 1 indicates that the average forward modelled data lies outside 2 standard deviations,  $2\sigma_i$ , from the observed phase velocity,  $d_i^{obs}$ . The starting model was a 60 x 0.33km layers, reaching a maximum depth of 20 km. Bootstrap resampling of the observations was then used to assess the uncertainty of the solution by randomly selecting observed phase velocities within the range defined by the mean and standard deviation. The distribution of the re-sampled solutions is used to estimate the uncertainty of the 1-D S-wave model.

### 3. Results

#### 3.1. Cross-correlations, phase velocity

The cross-correlations of the ambient noise recorded at each station-pair within the network shows a clear ~ 3km/s moveout, which is indicative of Rayleigh waves moving across the network (Figure 3).

Phase velocity analysis was performed at periods of 2.5s, 3.5s, 4.5s, 5.5s, 6.5s, and 7s (Figure 4). The median phase velocities for this selection of periods are 3.20 km/s, 3.16 km/s, 3.20 km/s, 3.19 km/s, 3.23 km/s, 3.21 km/s respectively (Figure 5). The decrease in phase velocity from 2.5s to 3.5s suggests the presence of a velocity inversion (i.e., a layer of rocks with a higher S-wave velocity above a layer with a slower velocity).

### **3.2. 2-D phase velocity maps**

Phase velocity tomography was performed for each period above. A selection of these phase velocity maps, with accompanying error estimates, are displayed in Figure 6. The phase velocities are plotted relative to the average phase velocity for the given period (e.g., 3.17 km/s for a period of 3.5 s). The resolution maps and residual plots for each period can be found in the Supplementary Information.

The phase velocity maps reveal lateral velocity variations that correspond with surface geology. For example, the phase velocity of a 2.5s wave shows a clear low velocity zone within the Kansanshi Mine of  $-0.27 \pm 0.08$  ( $2\sigma$ ) km/s relative to the average phase velocity of 3.21km/s (Figure 6A). This is contrasted with higher phase velocities of  $+0.08$  km/s immediately to the south of the mine. A velocity low is also seen within the mine at periods of 3.5s and 5.5s, with velocities of  $-0.22 \pm 0.06$  km/s and  $-0.12 \pm 0.09$  km/s respectively (Figure 6C, E). The area south of the mine is characterized by both velocity highs and velocity lows. This is particularly prevalent at a 5.5s period, with phase velocities ranging from  $-0.19 \pm 0.09$  to  $+0.05 \pm 0.09$  when moving south down the network, relatively to an average velocity of 3.18 km/s (Figure 6E). The average absolute amplitude bias along the network is 7.5 % at 2.5s, with an average of 7.0 % at 4.5s and 4.5 % at 7s. The average spatial resolution along the network is 2.4 km at 2.5s, rising to an average of 2.71 km and 3.6 km at 4.5s and 7s respectively (Supp. Figure 3-8).

### **3.3. 2-D S-wave cross-section**

The phase velocity maps were compiled into 60 dispersion curves along the X-X' profile of Figure 7A, each of which was inverted for a 1-D S-wave velocity profile. The sensitivity kernels of the included surface waves (2.5–7 s) demonstrate that the surface waves are sensitive to variations in S-wave velocity (~ lithology) down to depths well in excess of 10 km (Figure 5B). Bootstrap resampling of the dispersion curves was conducted over 500 iterations to evaluate the spread of potential S-wave models at each point along the profile. The re-sampling assumed a Gaussian distribution with a mean and standard deviation equal to that calculated in the phase velocity tomography for each period. The resulting S-wave cross-section displays the median and interquartile range of the distribution of solutions from the bootstrap re-samples (Figure CROSS). Given the non-Gaussian nature of the probability density function in non-linear problems, percentile-based confidence intervals such as the interquartile range are often more informative than the standard deviation (Menke, 1984).

The cross-section shows clear variations in S-wave velocity vertically and laterally along the profile. Beneath Kansanshi Mine at  $12.1^\circ\text{S}$ , the S-wave velocity drops from a high of 4.0 km/s at a depth of 1.5 km to a 3.11 km/s at a depth of 4.5 km. This low velocity zone is laterally continuous but rises to a shallower depth of 3.0 km and 3.2 km in the north and south respectively. The southern section of the profile is characterized by higher velocities.

For example, between latitudes of 12.25°S and 12.34°S, the average velocity at 4.5 km depth is 3.45 km/s while inside the Kansanshi Mine license, the average velocity at that depth is 3.22 km/s. However, the southern-most end exhibits another low velocity zone of 3.2 km/s at a depth of 2.2 km. These velocity contrasts are deemed robust because their velocity values remain distinct even when accounting for uncertainty (Figure 7C). The highest uncertainty is found within the Kansanshi Mine license, with an interquartile range of 0.45 at a depth of 2.3 km at -12.1°S. The average interquartile range above 10 km is 0.06 km/s.

## 4. Discussion

### 4.1. *The geological structure of the Kansanshi Cu-Au mine*

The S-wave cross-section demonstrates that the tomography successfully differentiates rock units with varying S-wave velocities, resulting in geologically realistic structures. Although the interpretation of S-wave velocities is non-unique, we assume that Katangan sediments have S-wave velocities up to 3.2 km/s as sandstones and mudstones have been measured to have S-wave velocities up to and exceeding this value (e.g.,  $3.26 \pm 0.18$  km/s for fine sandstone in Zhang et al., 2009). In contrast, lithologies with S-wave velocities above 3.3 km/s are interpreted as either basement or Lufilian-age metamorphics, because crystalline rocks—including granites, gneisses, and high-grade metamorphics—typically exhibit S-wave velocities ranging from 3.3 to 4.5 km/s (Christensen, 1996). Some overlap in S-wave velocities between Katangan sediments, basement, and metamorphic units is expected due to variations in composition, alteration, metamorphism, and deformation intensity. Therefore, lithologies with S-wave velocities between 3.2 km/s and 3.3 km/s could readily correspond to either sedimentary or basement/metamorphic units. We assign a velocity of 3.3 km/s as the pivot point in the color scheme of Figure 7A, 8A. This approach provides a practical balance, allowing for an approximate yet visually effective differentiation between these lithological categories.

It should be noted that surface waves have a relatively poor vertical resolution (Figure...). The S-wave models vary smoothly with depth, and therefore no discrete interfaces are observed. As such, the depths to structures such as the sediment-basement contact are poorly understood. However, the models do robustly show a large accumulation of sediments beneath Kansanshi. This is in good agreement with MacIntyre (2019) and Day & Tosca (2020) who previously identified significant sediment thickness ( $> 1.5$  km) beneath Kansanshi on the basis of deep sedimentary core logs. The sediment package appears to thin to the north and the south, and the depth of the sediment-basement contact also decreases away from the mine. This indicates the existence of a Lower Roan depocentre beneath the mine. The thinning of the sediments to the south is observed by Arthurs (1974) and is corroborated by the MS300 core log (Daly & Tosca, 2020). These lateral thickness variations are best explained by a graben system beneath Kansanshi (Figure 8B). The topography of the interface is likely controlled by original basin structures, such as normal faults, and later thrust faulting. To the south of the mine between -12.25°S and -12.35°S there are no velocities of 3.2 km/s and below. We interpret this area as a block of basement brought up along an out-of-sequence thrust, cutting the Katangan sediments and overlying metamorphic sheet. This is in good agreement with the surface geology, with the basement Solwezi Dome cropping out in this area (Figure 2). Sitting structurally above the sediments in much of the model is a layer of high-Vs rocks which we interpret as belonging to an

overthrust metamorphic sheet. This is in good agreement with the field observations, with garnet-biotite schists seen within the Kansanshi Mine and surrounding area (Barron, 2003; Daly & Tosca, 2020).

#### **4.2. *The mineral system at Kansanshi***

As previously noted, Hitzman et al. (2010) notes four fundamental controls on the formation of sedimentary metal deposits: 1) the presence of metal source sediments, 2) the presence of reduced sediments to serve as chemical traps, 3) saline brines for leaching and transporting metals, and 4) the expulsion of mineralizing fluids through focused zones. Each of these will be dealt with separately in the following section.

The Kansanshi deposit exhibits some key characteristics outlined in the Hitzman et al. (2010) model for sediment-hosted copper deposits but also diverges from the model in significant ways. This study does not provide direct evidence for reduced sediments acting as chemical traps, nor does it confirm the presence of saline brines, which are typically essential for metal transport. However, the S-wave model shows a large body of sediments beneath the Kansanshi Mine. This significant thickness of sediments would have provided a significant source of copper for scavenging and subsequent deposition within the Kansanshi deposit. This aligns with the idea that a large volume of metal-rich sediments is a prerequisite for forming a major copper deposit, following the red-bed source model of Hitzman (2000). The volume from which metal is sourced is a fundamental control on the probability of forming a large metal deposit (McCuaig & Hronsky, 2014). The ANT results also reveal fault systems and an antiformal structure beneath Kansanshi, which could have served as conduits for mineralizing fluids. Faults are well-documented pathways for hydrothermal fluids, and the structural geometry detected in this study suggests that deformation played a key role in localizing mineralization. The largest fault zone is the thrust faults bounding the Solwezi Dome. These faults may have been a conduit for the metasomatic fluids responsible for the formation of the whiteschists found at the boundary between the sediments and the Dome (Eglinger et al., 2014). Normal faulting and subsequent reactivation as thrust faults are expected beneath the Kansanshi Mine in order to explain the significant thickness of sediments which are not observed in outcrop to the south of the mine. These faults may well have acted as significant fluid pathways. Secondly, the S-wave model suggests the presence of a mild antiform directly beneath Kansanshi. This is consistent with the surface geology, as Kansanshi comprises a weakly dipping, NW-SE trending dome (e.g., MacIntyre, 2019). This antiformal structure would have provided the perfect trap structure for metal-bearing fluids. Finally, the S-wave model predicts the presence of an overlying metamorphic sheet which is clearly observed in the field. Daly & Tosca (2020) proposed that the overthrusting of the metamorphic sheet resulted in overpressuring of the underlying Katangan sediments in response to the increased overburden. This increase in pressure is calculated to have increased the solubility of chalcopyrite in the pore fluids and thus driven a significant Cu-enrichment in the circulating fluid (Daly & Tosca, 2020). Upon orogenic collapse and uplift, the overpressuring drove critical failure in the overlying sediments and the deposition of the Cu-rich veins for which Kansanshi is famous.

#### **4.3. *The application of ANT and MEMS accelerometers to mineral exploration***

As discussed above, it has long been known that ANT provides quality subsurface information at regional-continental scales using highly sensitive, complex-to-deploy, expensive broadband seismometers. Studies in recent years have also demonstrated the suitability of ANT for highly specific, local studies of mineral sites and other areas of geological interest (e.g., Colombero et al., 2022; Stork et al., 2018). The results demonstrate that relatively cheap, easy-to-use, quick-to-deploy MEMS accelerometers can be used to perform ANT and provide information at a greater lateral scale and depth than previously imaged in this type of environment. The workflow is readily applied to 3D surveys, with the lateral extent controlled by the dimensions of the seismometer array. The results from this study, such as the imaged significant thickness of sediments underlying the Kansanshi Mine, are corroborated by existing geological constraints (e.g., Daly & Tosca, 2020). The results demonstrate the ability of ANT to reliably detect lateral seismic velocity contrasts at depths of multiple kilometres, which would provide essential constraints for mineral exploration. The ANT and nodal seismometer combined workflow offers a number of advantages to the mineral exploration community - it is cheap compared to active source methods (vibroseis or explosions), the deployment of nodal arrays is quick and logistically easy, data processing can be readily automated, and the results are clear to interpret.

#### ***4.4. Limitations of the approach***

Although the S-wave cross-section demonstrates that ANT successfully differentiates rock units with varying S-wave velocities, resulting in geologically realistic structures, the approach has several limitations of import:

**The two-step inversion:** The methodology relies on a two-step inversion process—phase velocity tomography followed by an S-wave inversion. It is difficult/impossible to reliably understand 3-D uncertainty and resolution using a two-step method (Latallerie et al., 2024). Additionally, each step introduces its own set of assumptions and potential sources of error. For example, the phase velocity inversion relies upon sensitivity kernels that assume linear changes in velocity through space (Zhou et al., 2004). This means that discrete structures like fault zones are poorly resolved. The S-wave inversion is affected by the inherent non-uniqueness of the non-linear inversion process, meaning that multiple subsurface models could explain the observed data.

**The noise sources:** Cross-correlations provide an estimate of the empirical Green's Function when the noise sources are homogeneously distributed around the station pair (Weaver & Lobkis, 2001). As such, heterogeneous noise sources can be a source of bias in the phase velocity calculations. This may be of particular importance in areas around mine sites where several large noise sources (such as mine blasts) can be expected. In our case, the noise of Kansanshi Mine was a useful source as it lay along strike of the linear array. In a more 3-D network, this may not have been the case. Additionally, some studies have estimated that heterogenous noise sources impart only a small bias onto the phase velocity calculations (< 1 % in the case of Yao & van der Hilst, 2009).

**Vertical resolution of surface waves:** One of the fundamental limitations of ANT is the relatively poor vertical resolution of surface waves compared to body-wave methods and the difficulty in reliably understanding this resolution. Surface waves provide excellent lateral coverage, but their depth resolution is inherently limited by the frequency content of the recorded ambient noise and the breadth of the sensitivity kernels with depth (Figure 5B).

This makes it challenging to distinguish between closely spaced geological layers or to precisely define geological contacts and the thickness of rock units.

## 5. Conclusions

At the outset of this study, we posed two key questions: (1) To what extent does the Kansanshi deposit align with the conditions outlined in the Hitzman et al. model? (2) Could Ambient Noise Tomography (ANT) have identified the Kansanshi deposit without prior constraints? To test these questions, a network of 30 Sercel WiNG MEMS accelerometers was deployed along a c. 50 km long, linear transect through the Kansanshi Cu-mine and Solwezi, Zambia between October 2021 and May 2022, for a total of 188 days. ANT was performed using a two-step inversion – a phase velocity tomography following Forshaw & Lin (2005) followed by an S-wave inversion following Harmon & Rychert (2016). The resulting S-wave model, resolvable to at least 10 km depth, revealed key geological structures including an antiformal depocenter of Katangan sediments beneath the Kansanshi Mine, an uplifted basement section south of the mine, and an overlying metamorphic sheet. While the model's vertical resolution is limited, the sediment package likely thins north and south of the mine, with fault-controlled boundaries.

We conclude that Kansanshi shares some fundamental characteristics with sediment-hosted copper deposits, particularly in terms of its metal source and structural controls. However, it also exhibits key differences that suggest a more complex formation history, such as the presence of its Cu-rich, metre-scale, cross-cutting veins, which indicate that later-stage deformation and fluid remobilization played a major role in mineralization. The ANT results suggest a complex geological history, highlighted by the identification of the overlying metamorphic sheet and the out-of-sequence exhumation of the Solwezi Dome.

The results of this study suggest that ANT could have played a crucial role in identifying Kansanshi as a promising exploration target, even without prior geological constraints. The S-wave velocity model successfully detected: (1) A significant sedimentary depocenter beneath Kansanshi, which would indicate a potential metal source. (2) A structural high (antiformal feature), which could have served as a trap for mineralizing fluids. (3) Major fault systems, which are often conduits for hydrothermal fluid flow. These features align with key indicators of sediment-hosted copper deposits, meaning that ANT would have marked Kansanshi as a geologically significant area warranting further investigation. Consequently, we conclude that despite the documented limitations of the method, ANT is a particularly valuable tool for sub-regional mineral exploration. To mitigate the limitations of the method, we suggest quantitatively integrating ANT studies with complementary geophysical datasets such as gravity, Rayleigh-wave ellipticity, receiver functions, and body-wave tomography.

## Acknowledgements

T. Mackay-Champion would like to thank BHP and an Oxford-Radcliffe Graduate Scholarship for supporting his PhD research at the University of Oxford. Michael C. Daly would like to acknowledge funding from NERC CuBES WP1 Reference No. NE/T003170/1.

## Figures

Fig 1. Tectonic map of the Central African Copperbelt after Kounoudis et al. (2024). The black polygon demarcates the study area.

Fig. 2. Deployment map. The geological basemap is after Barron (2003).

Fig. 3. Station-pair cross-correlation moveout.

Fig 4. Average phase velocities for each period of interest and a comparison between the phase calculated for a zero-order Bessel Function (red dots) of the first kind and the observed phase of the real (symmetric) component of all the cross-correlations (blue dots). (A) Residuals plot for 2.5s, (B) Bessel Function comparison for 2.5s. (C, D) for 3.5s. (E, F) for 6.5s, (G, H) for 3.5s, (I,J) for 5.5s, (K,L) for 7s.

Fig 5. (A) Distribution of phase velocities at each period. Boxplots show the median value, the interquartile range and maximum and minimum values defined as 1.5 times the interquartile range away from the bottom or top of the box. (B) Depth sensitivity kernels for the surface waves of interest.

Fig 6. 2-D phase velocity models. The phase velocities are plotted relative to the average phase velocity ( $\bar{c}$ ) for the given period. (A) Phase velocity map for a period of 2.5s. (B) Phase velocity error map for a period of 2.5s. (C, D) for a period of 3.5s. (E, F) for a period of 5.5s.

Fig 7. 2D S-wave model. (A) Location of points along the profile. (B) S-wave velocity model corresponding to the points in (A). (C) S-wave velocity uncertainty defined as the interquartile range.

Fig 8. Tectonic interpretation. (A) 2D S-wave velocity model. (B) Geological interpretation.

## References

Arthurs, J. W. (1974). *Geology of the Solwezi Area, Degree Sheets 1226, NW Quarter and 1126 SW Quarter* (Issue 36). Government Printer.

Bakun, N. N., Volodin, R. N., & Krendelev, F. P. (1966). Genesis of Udkansk cupriferous sandstone deposit (Chitinsk oblast). *International Geology Review*, 8(4), 455–466. <https://doi.org/10.1080/00206816609474302>

Barron, J. (2003). *The Stratigraphy, Metamorphism and Tectonic History of the Solwezi Area, Northwest Province, Zambia: Integrating Geological Field Observations and Airborne Geophysics in the Interpretation of Regional Geology* [PhD]. Colorado School of Mines.

Bensen, G. D., Ritzwoller, M. H., Barmin, M. P., Levshin, A. L., Lin, F., Moschetti, M. P., Shapiro, N. M., & Yang, Y. (2007). Processing seismic ambient noise data to obtain reliable broad-band surface wave dispersion measurements. *Geophysical Journal International*, 169(3), 1239–1260. <https://doi.org/10.1111/j.1365-246X.2007.03374.x>

Christensen, N. I. (1996). Poisson's ratio and crustal seismology. *Journal of Geophysical Research: Solid Earth*, 101(B2), 3139–3156. <https://doi.org/10.1029/95JB03446>

Colombero, C., Papadopoulou, M., Kauti, T., Skyttä, P., Koivisto, E., Savolainen, M., & Socco, L. V. (2022). Surface-wave tomography for mineral exploration: a successful combination of passive and active data (Siilinjärvi phosphorus mine, Finland). *Solid Earth*, 13(2), 417–429. <https://doi.org/10.5194/se-13-417-2022>

Cosi, M., De Bonis, A., Goso, G., Hunziker, J., Martinotti, G., Moratto, S., Robert, J. P., & Ruhlman, F. (1992). Late proterozoic thrust tectonics, high-pressure metamorphism and uranium mineralization in the Domes Area, Lufilian Arc, Northwestern Zambia. *Precambrian Research*, 58(1–4), 215–240.  
[https://doi.org/10.1016/0301-9268\(92\)90120-D](https://doi.org/10.1016/0301-9268(92)90120-D)

Daly, Michael. C., & Tosca, N. (2020). A Geodynamic Model of the Kansanshi Cu-Au System, Zambia. *SEG Conference*.

Eglinger, A., Tarantola, A., Durand, C., Ferraina, C., Vanderhaeghe, O., André-Mayer, A. S., Paquette, J. L., & Deloule, E. (2014). Uranium mobilization by fluids associated with Ca-Na metasomatism: A P-T-t record of fluid-rock interactions during Pan-African metamorphism (Western Zambian Copperbelt). *Chemical Geology*, 386, 218–237.  
<https://doi.org/10.1016/j.chemgeo.2014.07.028>

Forsyth, D. W., & Li, A. (2005). Array Analysis of Two-Dimensional Variations in Surface Wave Phase Velocity and Azimuthal Anisotropy in the Presence of Multipathing Interference. In *Seismic Earth: Array Analysis of Broadband Seismograms* (pp. 81–97). American Geophysical Union (AGU). [https://doi.org/https://doi.org/10.1029/157GM06](https://doi.org/10.1029/157GM06)

Fougerat, A., Guérineau, L., & Tellier, N. (2018). High-quality signal recording down to 0.001 Hz with standard MEMS accelerometers. *SEG Technical Program Expanded Abstracts 2018*, 196–200. <https://doi.org/10.1190/segam2018-2995544.1>

Harmon, N., Gerstoft, P., Rychert, C. A., Abers, G. A., Salas de la Cruz, M., & Fischer, K. M. (2008). Phase velocities from seismic noise using beamforming and cross correlation in Costa Rica and Nicaragua. *Geophysical Research Letters*, 35(19).  
<https://doi.org/10.1029/2008GL035387>

Harmon, N., & Rychert, C. A. (2016). Joint inversion of teleseismic and ambient noise Rayleigh waves for phase velocity maps, an application to Iceland. *Journal of Geophysical Research: Solid Earth*, 121(8), 5966–5987.  
<https://doi.org/10.1002/2016JB012934>

Herrmann, P., Laroche, S., Wang, H., & Tellier, N. (2021). Land Acquisition without Data Jitter Made Possible with MEMS Sensors. *82nd EAGE Annual Conference & Exhibition*, 1–5. <https://doi.org/10.3997/2214-4609.202112510>

Herrmann, R. B. (2013). Computer programs in seismology: An evolving tool for instruction and research. *Seismological Research Letters*, 84(6), 1081–1088.  
<https://doi.org/10.1785/0220110096>

Hitzman, M., Kirkham, R., Broughton, D., Thorson, J., & Selley, D. (2005). The Sediment-Hosted Stratiform Copper Ore System. In *One Hundredth Anniversary Volume*. Society of Economic Geologists. <https://doi.org/10.5382/AV100.19>

Hitzman, M. W. (2000). Source basins for sediment-hosted stratiform Cu deposits: implications for the structure of the Zambian Copperbelt. *Journal of African Earth Sciences*, 30(4), 855–863. [https://doi.org/10.1016/S0899-5362\(00\)00056-7](https://doi.org/10.1016/S0899-5362(00)00056-7)

- Hitzman, M. W., Selley, D., & Bull, S. (2010). Formation of Sedimentary Rock-Hosted Stratiform Copper Deposits through Earth History. *Economic Geology*, 105(3), 627–639. <https://doi.org/10.2113/gsecongeo.105.3.627>
- Laine, J., & Mougenot, D. (2014). A high-sensitivity MEMS-based accelerometer. *The Leading Edge*, 33(11), 1234–1242. <https://doi.org/10.1190/tle33111234.1>
- Latallerie, F., Zaroli, C., Lambotte, S., Maggi, A., Walker, A., & Koelemeijer, P. (2024). Towards surface-wave tomography with 3D resolution and uncertainty. In *(in review)*. <https://doi.org/10.31223/X5FM79>
- Liu, H.-F., Luo, Z.-C., Hu, Z.-K., Yang, S.-Q., Tu, L.-C., Zhou, Z.-B., & Kraft, M. (2022). A review of high-performance MEMS sensors for resource exploration and geophysical applications. *Petroleum Science*, 19(6), 2631–2648. <https://doi.org/10.1016/j.petsci.2022.06.005>
- MacIntyre, T. J. (2019). *Geology and Geochemistry of the Kansanshi Cu-(Au) Deposit, North-Western Province, Zambia*.
- Marquardt, D. W. (1970). Generalized Inverses, Ridge Regression, Biased Linear Estimation, and Nonlinear Estimation. *Technometrics*, 12(3), 591. <https://doi.org/10.2307/1267205>
- McCuaig, T. C., & Hronsky, J. M. A. (2014). The Mineral System Concept: The Key to Exploration Targeting. In *Building Exploration Capability for the 21st Century*. Society of Economic Geologists. <https://doi.org/10.5382/SP.18.08>
- McKeith, T. D., Schodde, R. C., & Baltis, E. J. (2010). Gold Discovery Trends. *SEG Discovery*, 81, 1–26. <https://doi.org/10.5382/SEGnews.2010-81fea>
- Menke, W. (1984). *Geophysical Data Analysis: Discrete Inverse Theory*. Elsevier. <https://doi.org/10.1016/B978-0-12-490920-5.X5001-7>
- Okada, K. (2021). A Historical Overview of the Past Three Decades of Mineral Exploration Technology. *Natural Resources Research*, 30(4), 2839–2860. <https://doi.org/10.1007/s11053-020-09721-4>
- Reid, A., Olivier, G., & Jones, T. (2025). Ambient Noise Tomography: A Sensitive, Rapid, Passive Seismic Technique for Mineral Exploration. *SEG Discovery*, 140, 17–26. <https://doi.org/10.5382/SEGnews.2025-140fea-01>
- Sánchez-Sesma, F. J., & Campillo, M. (1991). Diffraction of P, SV, and Rayleigh waves by topographic features: A boundary integral formulation. *Bulletin of the Seismological Society of America*, 81(6), 2234–2253.
- Schlaphorst, D., Harmon, N., Kendall, J. M., Rychert, C. A., Collier, J., Rietbrock, A., & Goes, S. (2021). Variation in Upper Plate Crustal and Lithospheric Mantle Structure in the Greater and Lesser Antilles From Ambient Noise Tomography. *Geochemistry, Geophysics, Geosystems*, 22(7). <https://doi.org/10.1029/2021GC009800>

- Selley, D., Broughton, D., Scott, R., Hitzman, M., Bull, S., Large, R., McGoldrick, P., Croaker, M., Pollington, N., & Barra, F. (2005). A New Look at the Geology of the Zambian Copperbelt. In *One Hundredth Anniversary Volume*. Society of Economic Geologists. <https://doi.org/10.5382/AV100.29>
- Shapiro, N. M., Campillo, M., Stehly, L., & Ritzwoller, M. H. (2005). High-Resolution Surface-Wave Tomography from Ambient Seismic Noise. *Science*, 307(5715), 1615–1618. <https://doi.org/10.1126/science.1108339>
- Stork, A. L., Allmark, C., Curtis, A., Kendall, J.-M., & White, D. J. (2018). Assessing the potential to use repeated ambient noise seismic tomography to detect CO<sub>2</sub> leaks: Application to the Aquistore storage site. *International Journal of Greenhouse Gas Control*, 71, 20–35. <https://doi.org/10.1016/j.ijggc.2018.02.007>
- Tarantola, A., & Valette, B. (1982). Generalized nonlinear inverse problems solved using the least squares criterion. *Reviews of Geophysics*, 20(2), 219–232. <https://doi.org/10.1029/RG020i002p00219>
- Tellier, N., Laroche, S., & Herrmann, P. (2020). Native true amplitude and phase broadband sensing now available with the latest MEMS sensors. *SEG Technical Program Expanded Abstracts 2020*, 111–115. <https://doi.org/10.1190/segam2020-3423114.1>
- Vaughan, D. J., Sweeney, M. A., Friedrich, G., Diedel, R., & Haranczyk, C. (1989). The Kupferschiefer; an overview with an appraisal of the different types of mineralization. *Economic Geology*, 84(5), 1003–1027. <https://doi.org/10.2113/gsecongeo.84.5.1003>
- Watzel, R. (2023). Minerals for future technologies: how Germany copes with challenges. *Geological Society, London, Special Publications*, 526(1), 13–24. <https://doi.org/10.1144/SP526-2022-12>
- Weaver, R., & Lobkis, O. (2001). On the emergence of the Green's function in the correlations of a diffuse field. *The Journal of the Acoustical Society of America*, 109(5\_Supplement), 2410–2410. <https://doi.org/10.1121/1.4744516>
- White, E., & Hook, L. (2023, August 6). Miner Rio Tinto to test “new frontiers” as copper age dawns. *Financial Times*.
- Wood, A. D., & Hedenquist, J. (2019). Mineral Exploration: Discovering and Defining Ore Deposits. *SEG Discovery*, 116, 1–22. <https://doi.org/10.5382/Geo-and-Mining-02>
- Yao, H., & van der Hilst, R. D. (2009). Analysis of ambient noise energy distribution and phase velocity bias in ambient noise tomography, with application to SE Tibet. *Geophysical Journal International*, 179(2), 1113–1132. <https://doi.org/10.1111/j.1365-246X.2009.04329.x>
- Zhang, X., Tsang, L. L. H., Wang, Y., & Zhao, B. (2009). Petrologic composition model of the upper crust in Bohai Bay basin, China, based on Lamé impedances. *Applied Geophysics*, 6(4), 327–336. <https://doi.org/10.1007/s11770-009-0039-5>

Zhou, Y., Dahlen, F. A., & Nolet, G. (2004). Three-dimensional sensitivity kernels for surface wave observables. *Geophysical Journal International*, 158(1), 142–168.  
<https://doi.org/10.1111/j.1365-246X.2004.02324.x>

Figure 1 22°E

24°E

26°E

28°E

30°E

32°E

8°S

10°S

12°S

14°S

16°S

18°S

- I. External Fold-Thrust Belt
- II. Domes Region
- III. Synclinorial Belt
- IV. Katanga High

CONGO CRATON

Kibaran Belt

Lufilian Arc

STUDY AREA

BANGWEULU CRATON

Ubendian Belt

Luangwa Rift Zone

Irumide Belt

Mozambique Belt

Domes

Karoo Rifting

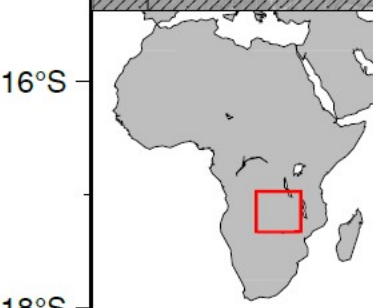
Hook Granite

MWSZ

Zambezi Belt

KALAHARI CRATON

CHOMA-KALOMO BLOCK

**Tectonic Context**

Mafics

Hook Granite

Karoo Rifting



Phanerozoic Sed.

Cratons

Paleoproterozoic Belts

Pan-African Lufillian Belt

Eclogite

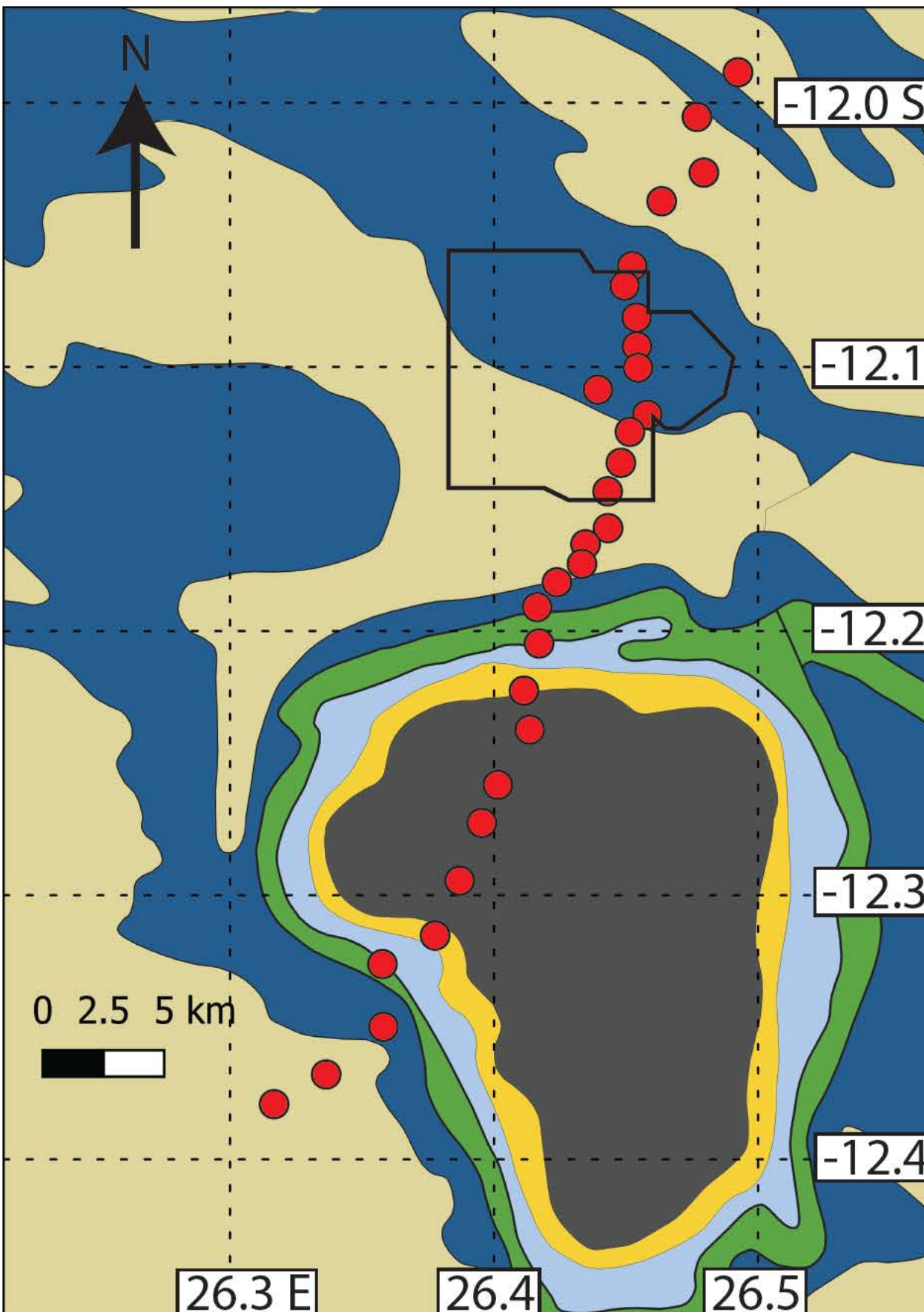
Domes

Mesoproterozoic Belts

Pan-African Zambezi Belt

Earthquakes

Figure 2



## KATANGA SUPERGROUP

Kundelungu
Nguba
Mwashia
Upper Roan
Lower Roan

□ Kansashi Mine license

● node locations

## BASEMENT

■ Basement

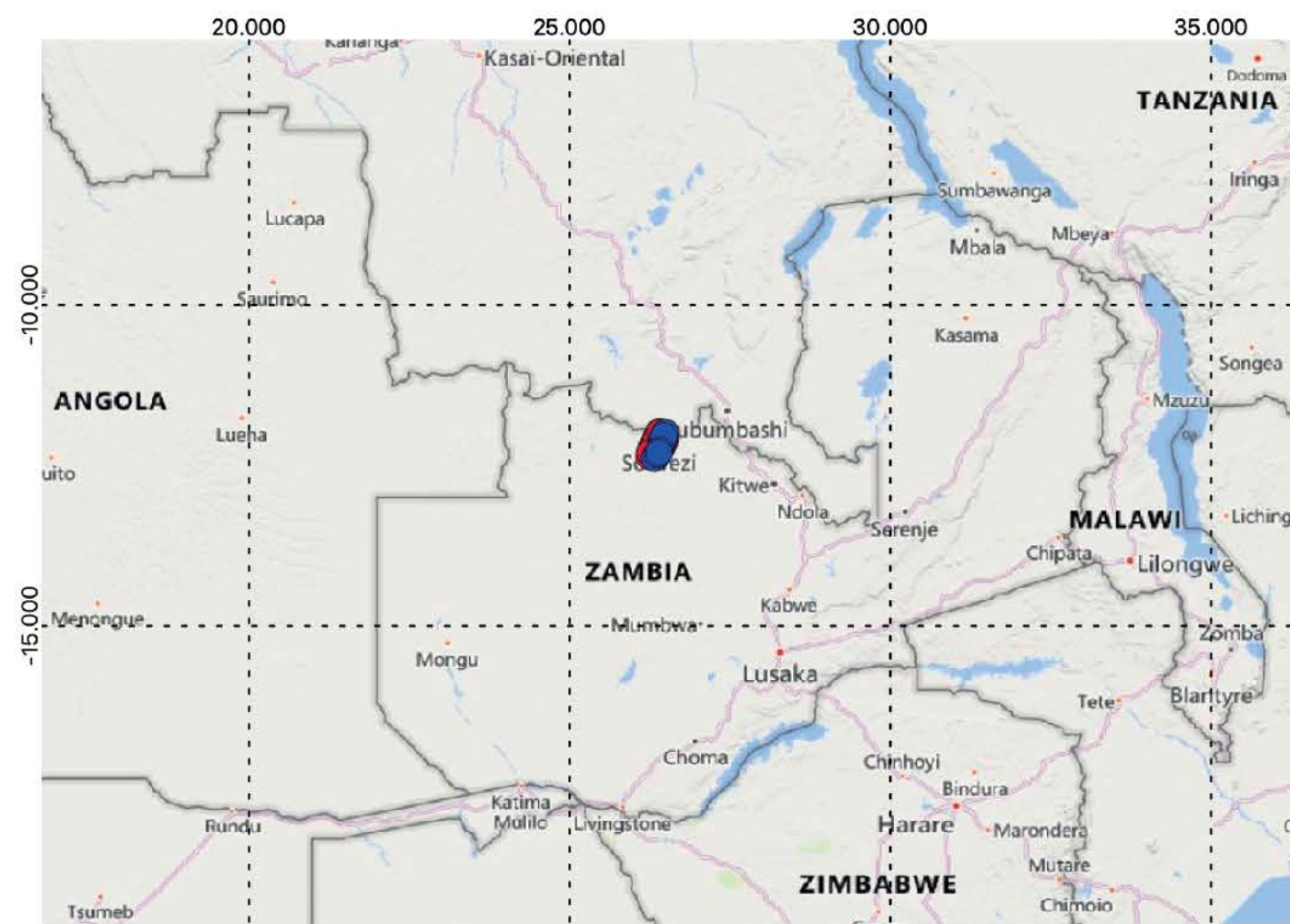
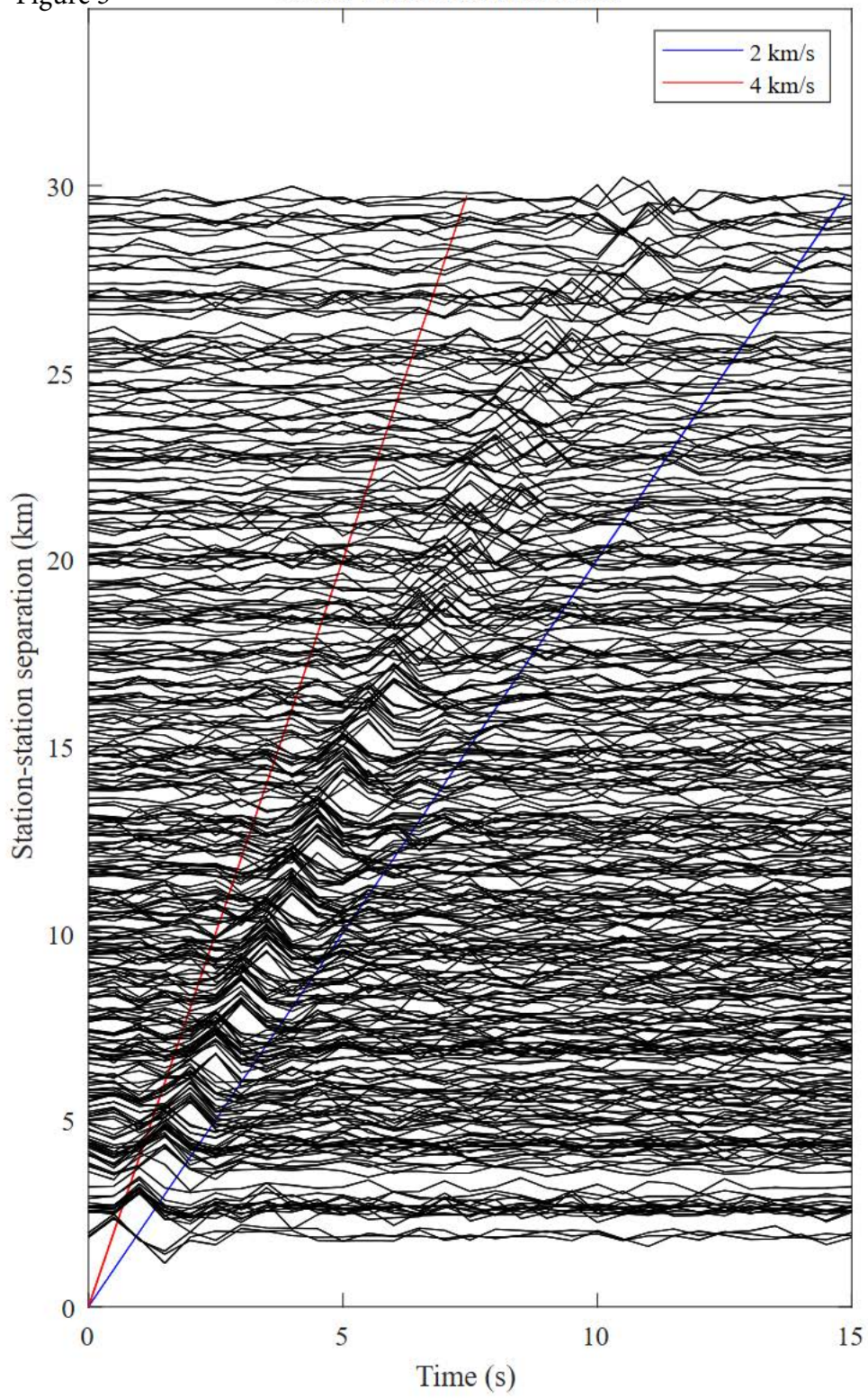


Figure 3

**Cross-correlation moveout**

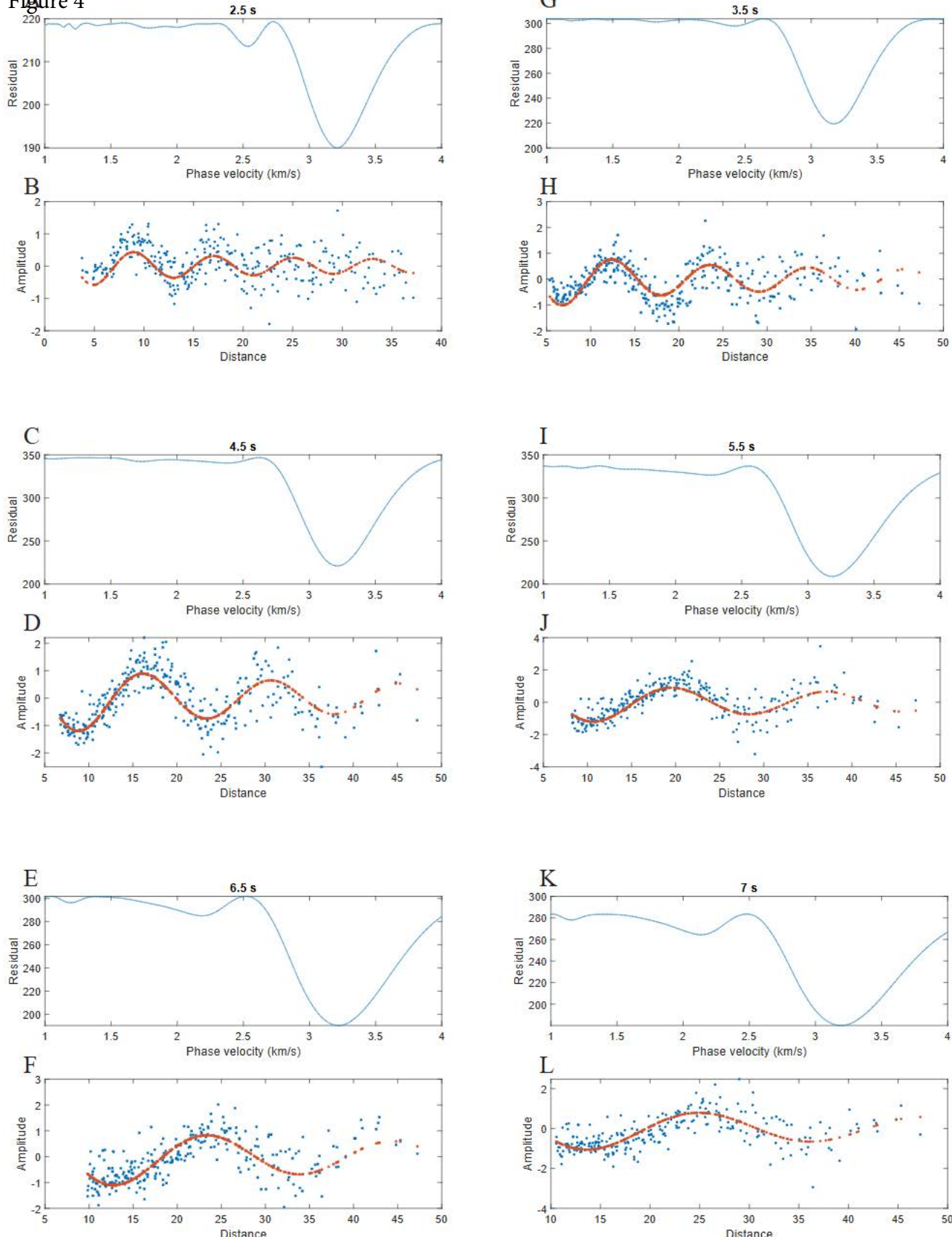
**Figure 4**

Figure 5

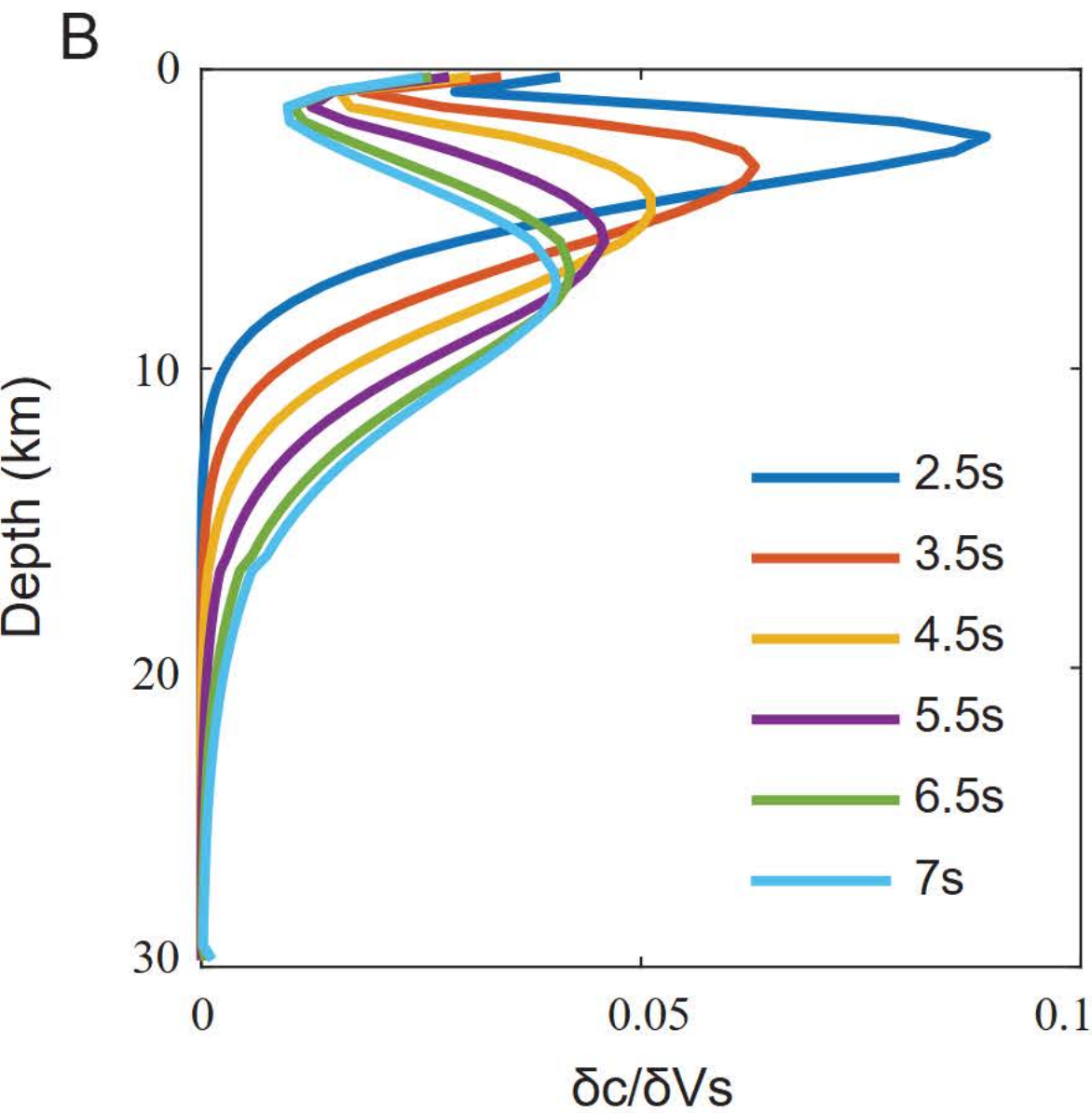
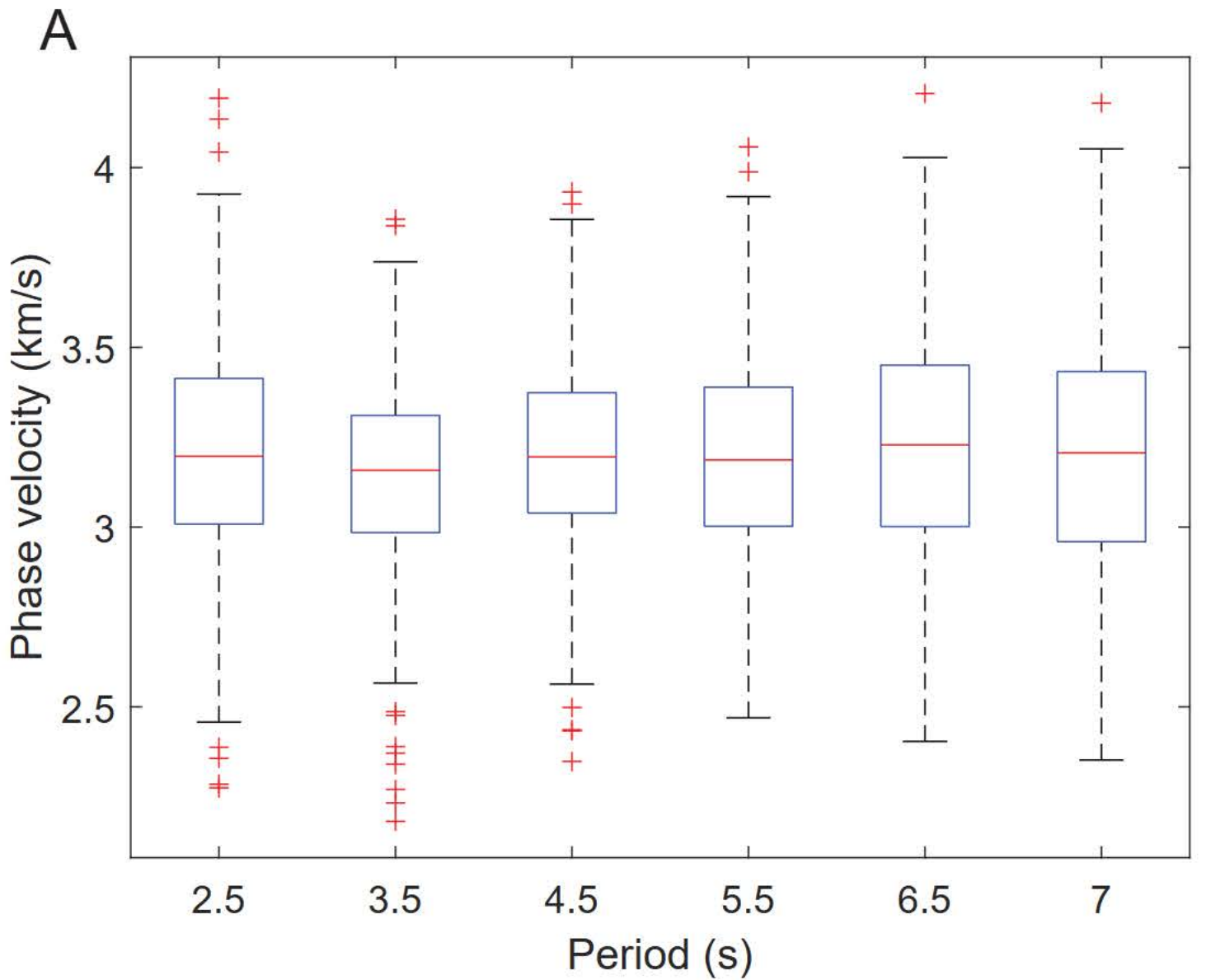


Figure 6

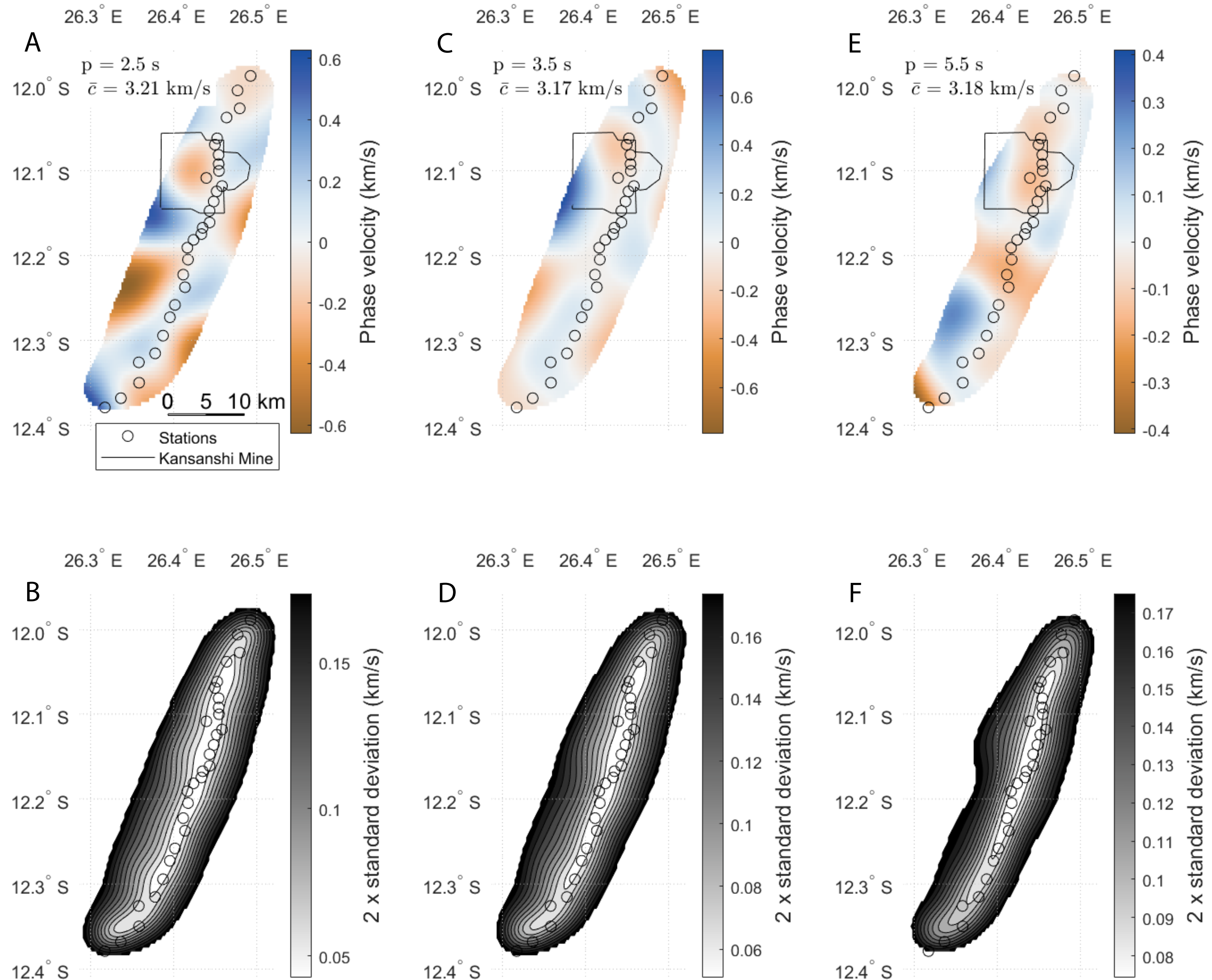


Figure 7

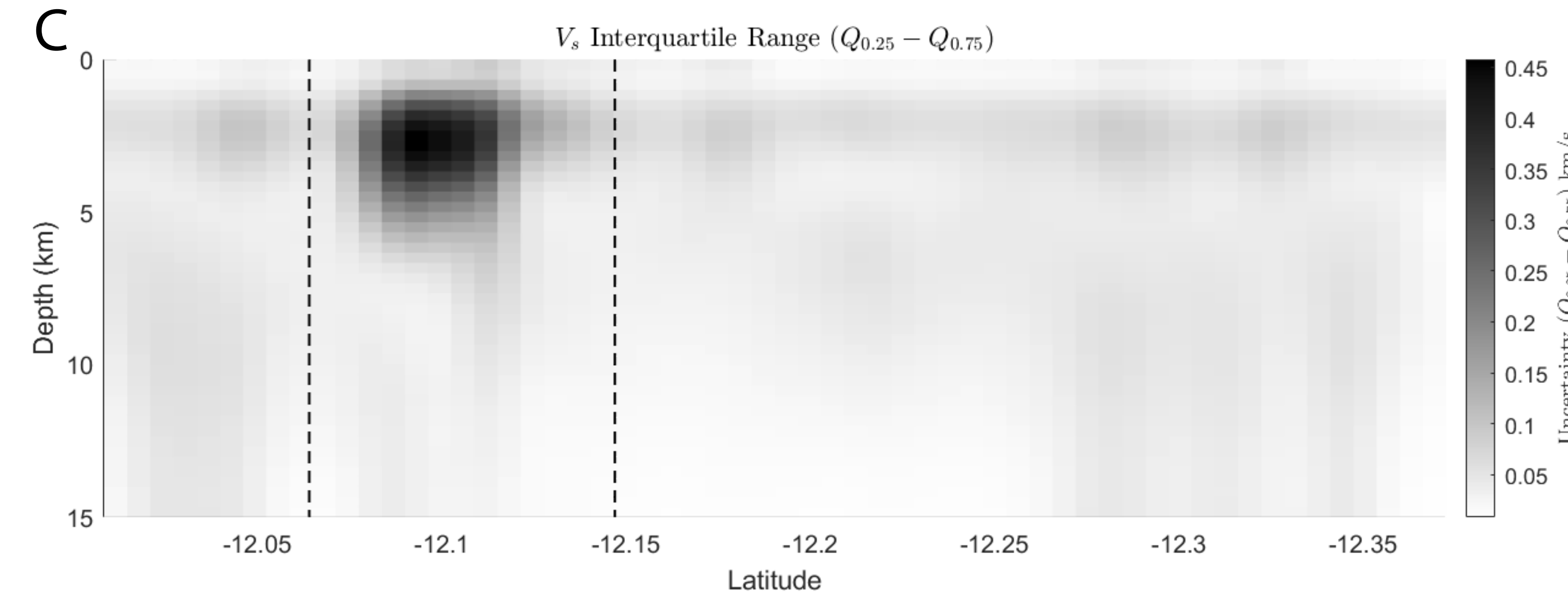
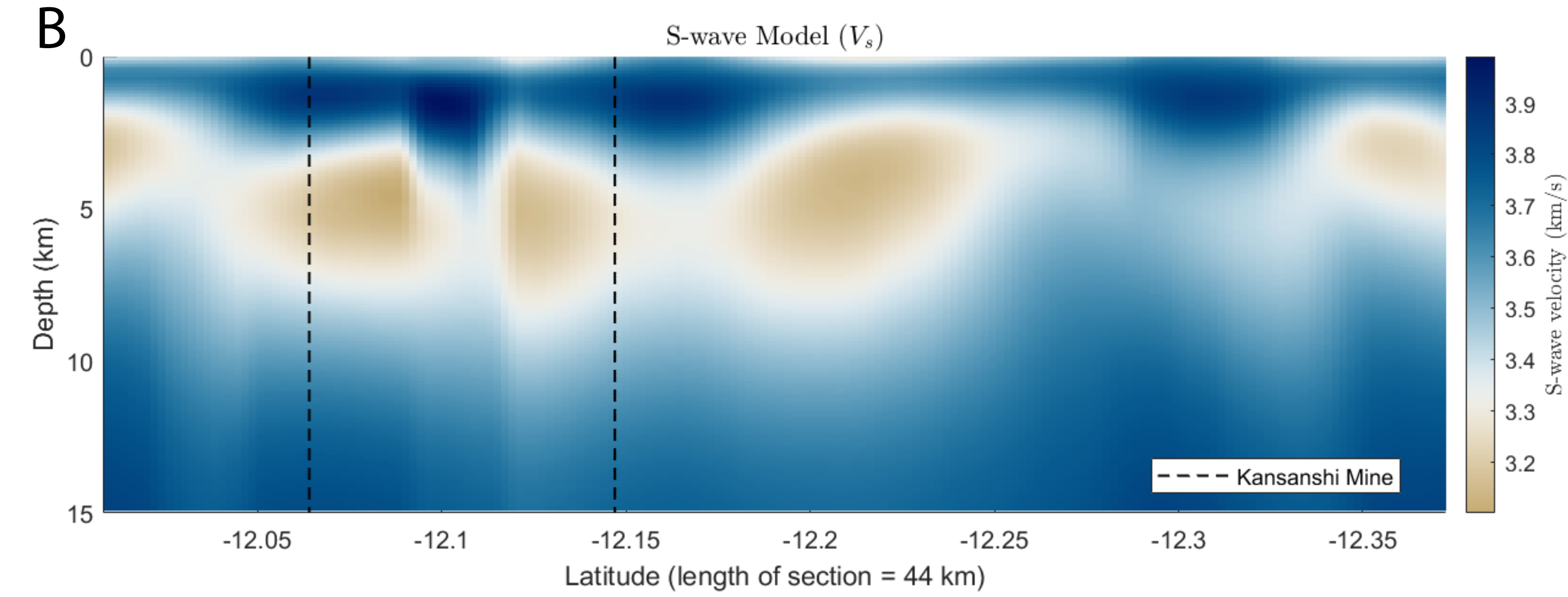
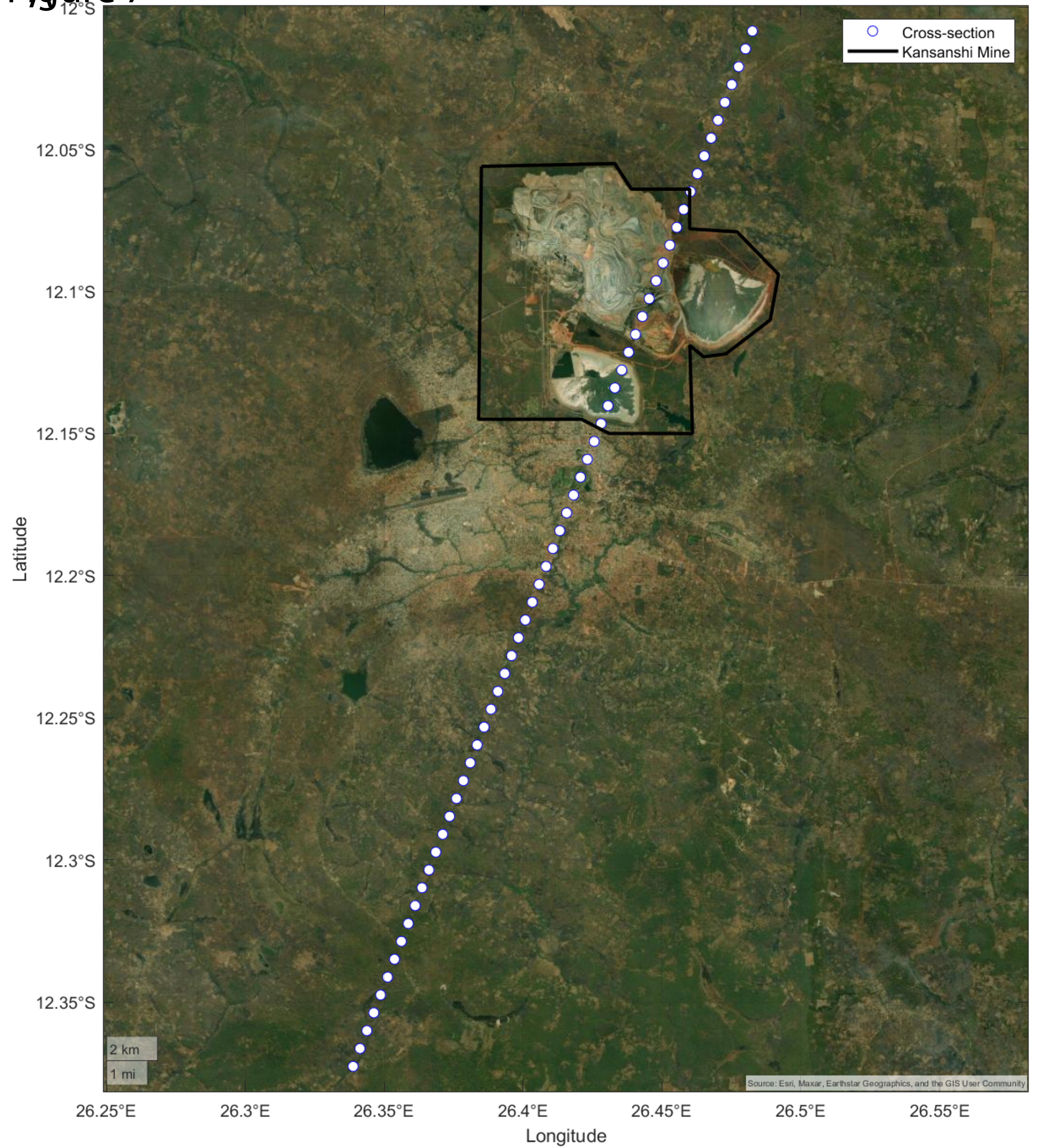
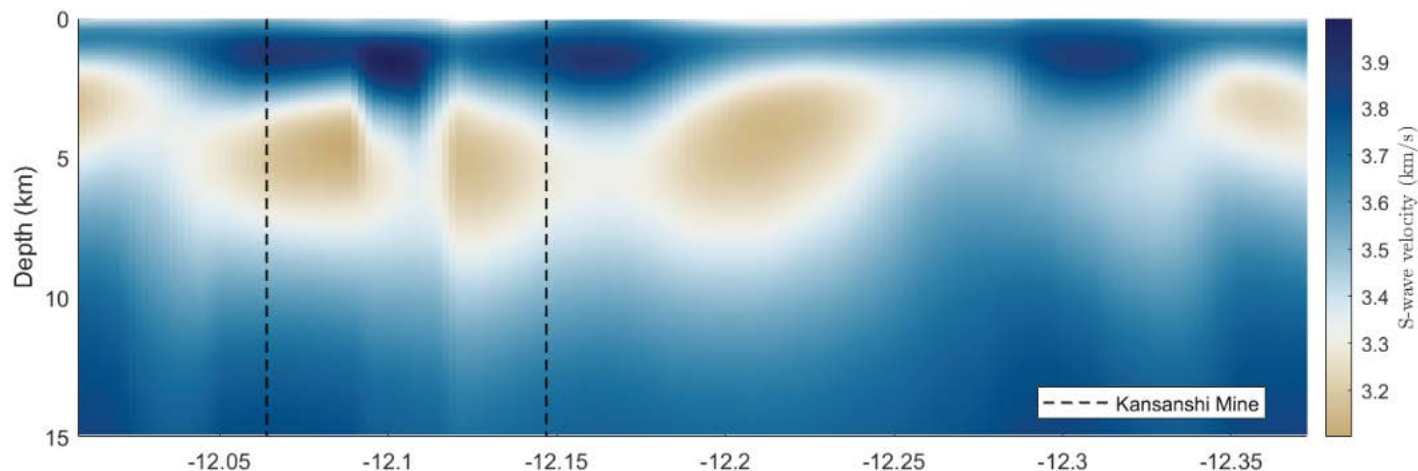
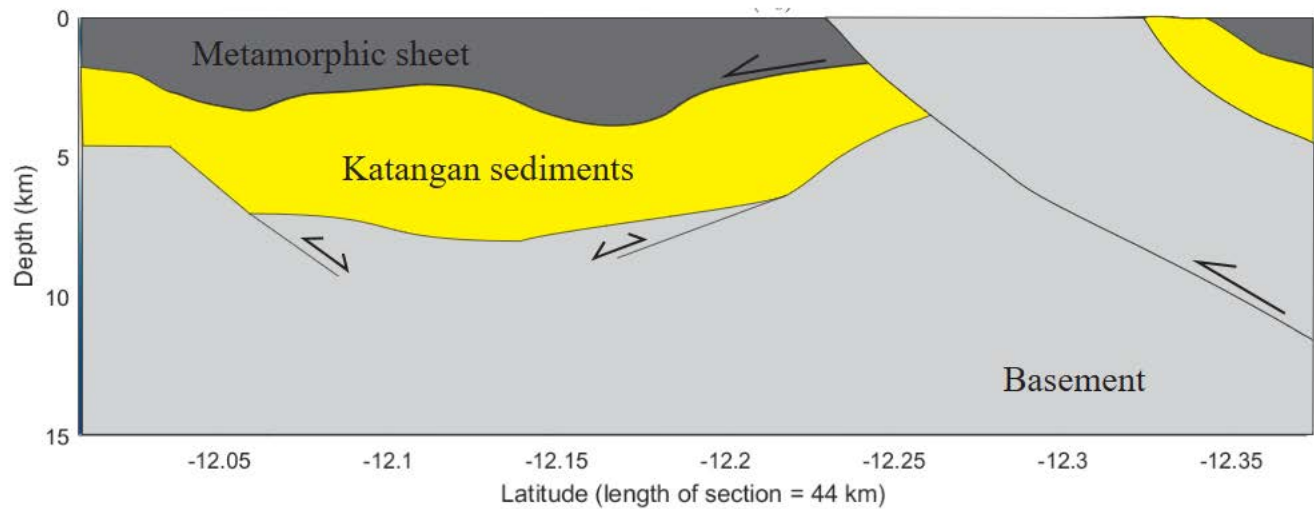


Figure 8



B



## SUPPLEMENTARY INFORMATION

### **Ambient Noise Tomography for Sub-Regional Mineral Exploration Using Nodal MEMS Accelerometers: A Case Study from the Kansanshi Cu-Au Mine, Zambia.**

T. Mackay-Champion<sup>1</sup>, N. Harmon<sup>2</sup>, S. Mutelekesha<sup>3</sup>, M. Chanda<sup>4</sup>, T. Hudson<sup>5</sup>, J.-M. Kendall<sup>1</sup>, M.C. Daly<sup>1</sup>.

1. Department of Earth Sciences, University of Oxford, South Parks Road, Oxford, UK.

2. Geology and Geophysics, Woods Hole Oceanographic Institution, Woods Hole, Massachusetts 02543, USA, Woods Hole Oceanographic Institute, USA.

3. First Quantum Minerals Ltd.

4. Geological Survey Department, Ministry of Mines, Zambia.

5. Institute of Geophysics, ETH Zürich, Switzerland.

#### **1. Error analysis**

Following Forsyth & Lin (2005), the variance of the inversion solution is found using linear error propagation (Clifford, 1975) and given by Equation 1.

$$\sigma_m^2 = \frac{q C_{MM} q^T}{\Sigma q} \quad (1)$$

$$C_{MM} = \left( G^T C_d^{-1} G + C_m^{-1} \right)^{-1} \quad (2)$$

Where  $C_{MM}$  is the complete, *a posteriori*, model covariance matrix and  $q$  are the weights used in the Gaussian model smoothing. The phase velocity residuals ( $\epsilon$ ) are calculated following Equation 3.

$$\epsilon = \frac{s}{p\phi_T} - \frac{s}{\left( 2\pi \frac{s}{pc} + G(m - m_0) \right) \cdot p} \quad (3)$$

#### **2. Resolution estimates**

We follow the method outlined in Barmin et al. (2001) for quantifying the spatial resolution and amplitude bias of the tomography. The resolution matrix is defined in Equation 4.

$$R = \left( G^T C_d^{-1} G + C_m^{-1} \right)^{-1} G^T C_d^{-1} G \quad (4)$$

Where each row of  $R$  is equivalent to a map defining the resolution for a particular node in the model. For each row, we fit a cone to the map. The width of the cone halfway to the bottom is taken as the spatial resolution (Ritzwoller et al., 2002).

The amplitude resolution is estimated using Equation 5. For each node in the velocity model, we apply the appropriate row of the resolution matrix to a test model ( $m$ ) consisting of a

cylinder of unit height with a diameter equal to twice the spatial resolution ( $2\sigma_R$ ) at the node point. The estimated amplitude of the fit surface ( $\hat{m}$ ) is the average amplitude within  $\sigma_R$  of the centre of the cylinder. The amplitude bias estimate is the relative difference between the input amplitude and the estimated amplitude.

$$\hat{m} = Rm \quad (5)$$

### 3. Phase velocity tomography trade-off

The trade-off analyses plot the sum of the absolute residuals against the model length.

#### Model damping trade-off

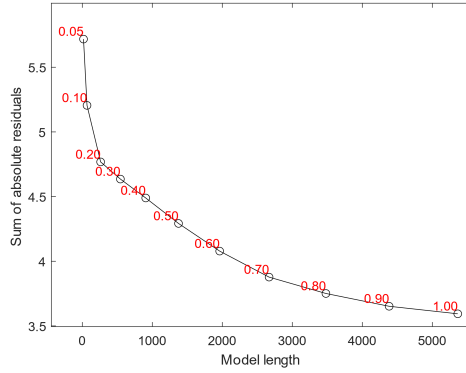


Figure 1

#### Characteristic length trade-off

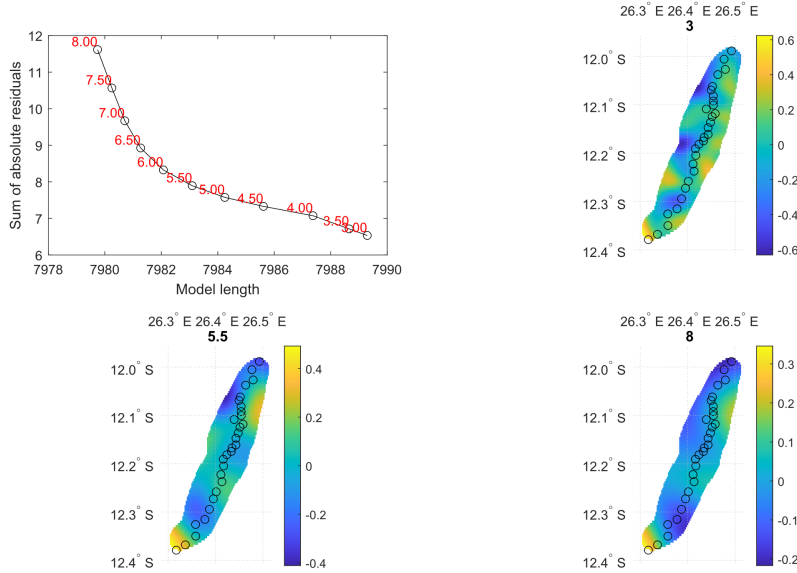


Figure 2

#### 4. Phase velocity maps with accompanying resolution and error estimates.

Period 2.5s

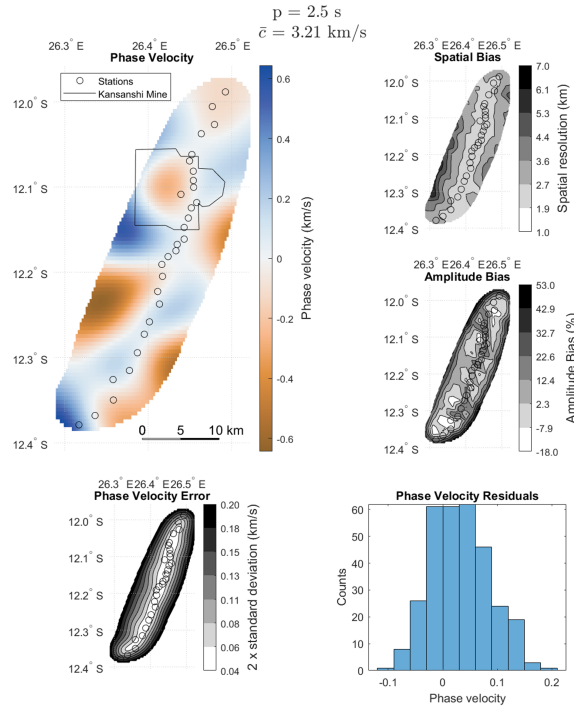
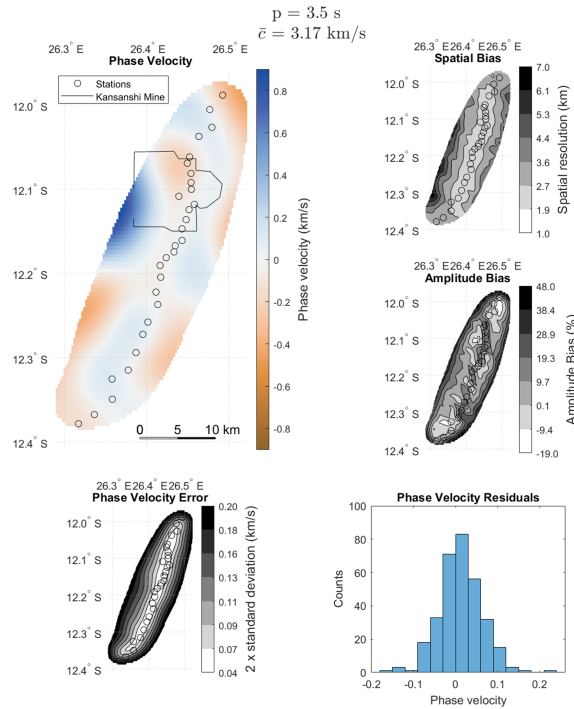
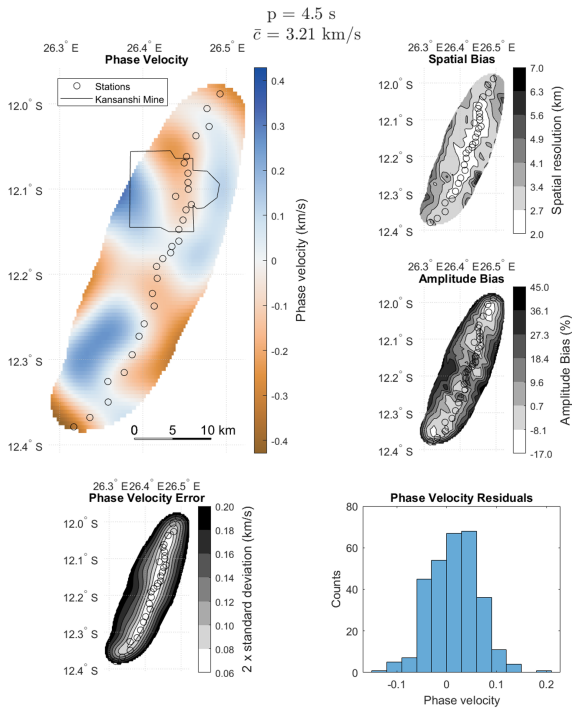


Figure 3

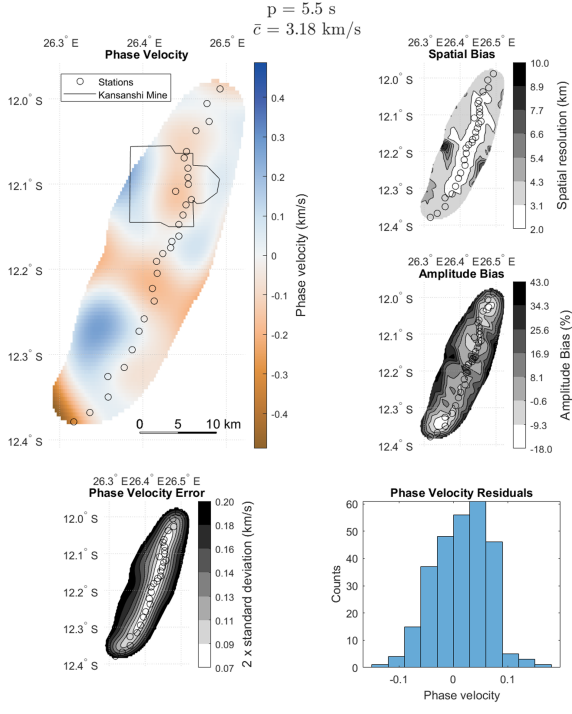
Period 3.5s



## Period 4.5s



## Period 5.5s



### Period 6.5s

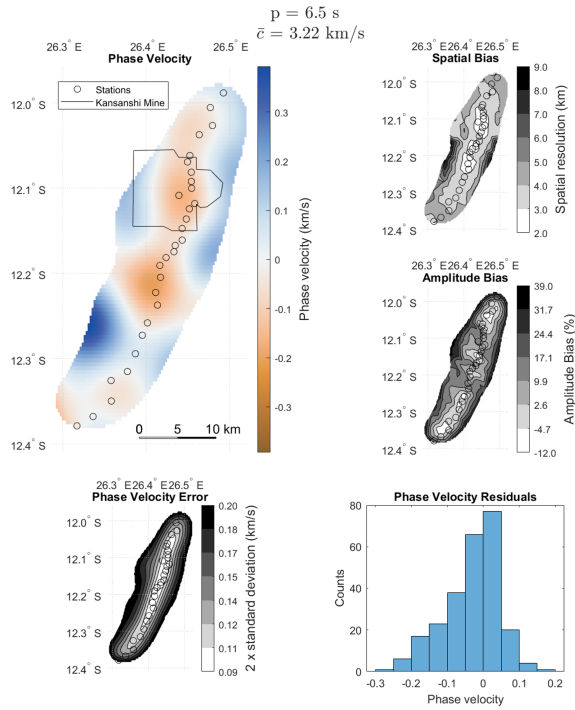


*Figure 7*

### Period 7s

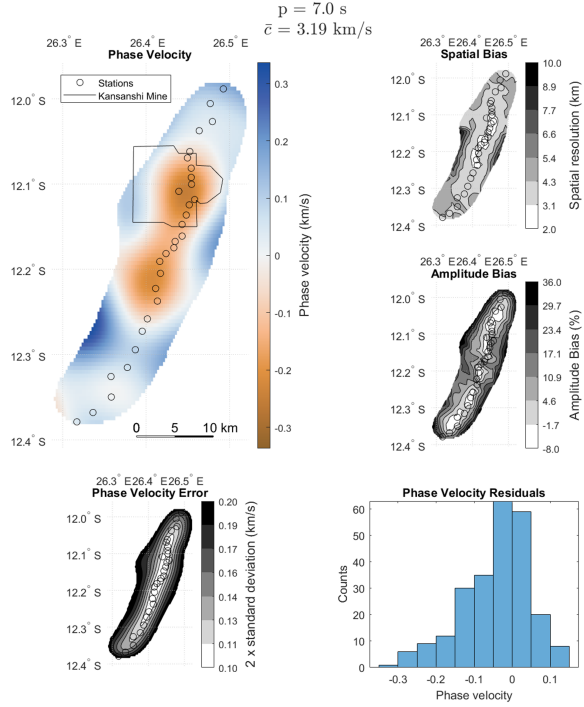


*Figure 8*

## 5. S-wave inversion trade-off

A damping parameter was selected which minimized the length of the solution ( $L$ ) while still fitting the data.

$$L = (\mathbf{m} - \bar{\mathbf{m}})^T(\mathbf{m} - \bar{\mathbf{m}})$$

Where  $\mathbf{m}$  is the model vector and  $\bar{\mathbf{m}}$  is the mean of the model vector. A value of 0.1 was chosen for the damping parameter as it represents the knee of the trade-off curve between the spread of the resolution matrix and the solution length (Figure 9). A chi-value of less than 1 indicates that the model fits the observed data.

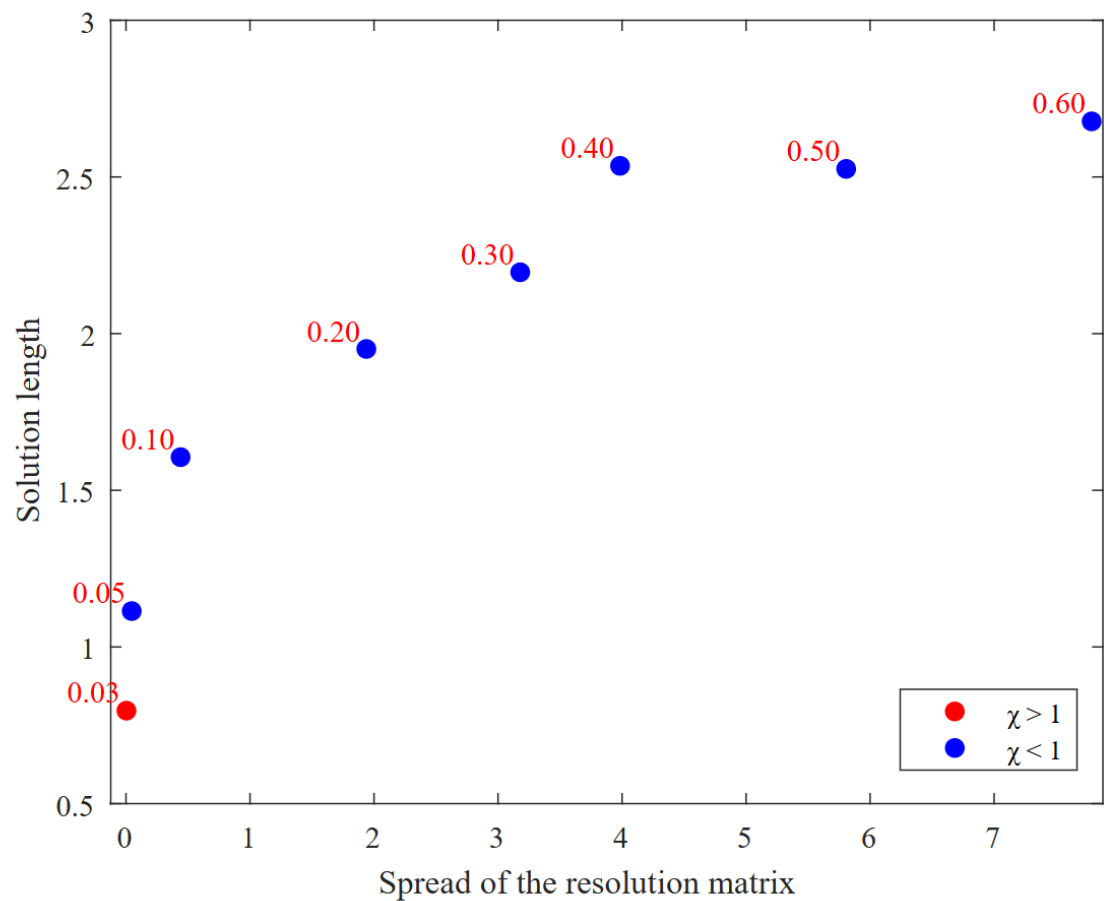


Figure 9